Materials & Design 237 (2024) 112596

Contents lists available at ScienceDirect

Materials & Design

journal homepage: www.elsevier.com/locate/matdes

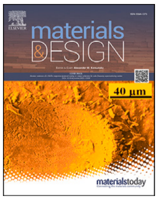

Studying the effects of Nb on high-temperature deformation in TiAl alloys using atomistic simulations

Anju Chandran [a], Hariprasath Ganesan [a,b,*,1], Christian J. Cyron [a,c]

[a] Institute of Material Systems Modeling, Helmholtz-Zentrum Hereon, Geesthacht, Germany
[b] Institute for Advanced Simulations – Materials Data Science and Informatics (IAS-9), Forschungszentrum Juelich, Juelich, Germany
[c] Institute for Continuum and Material Mechanics, Hamburg University of Technology, Hamburg, Germany

ARTICLE INFO

Keywords:
TiAlNb alloy
Molecular dynamics
Density functional theory
Nanomechanics
Ductility
Strength

ABSTRACT

Intermetallic γ(TiAl)-based alloys find their application as high-temperature materials for aero engine and automotive components. Microstructure optimization and microalloying play key roles in optimizing these alloys. Several pioneering experimental works showed improved mechanical properties of γ(TiAl)-based alloys containing Niobium (Nb). Despite Nb being a key alloying element, its contribution remains debated, if not least understood, due to the TiAl microstructure's complexity with hierarchical interfaces. This work examines the effects of Nb on the high-temperature deformation behavior of TiAl alloys using atomistic simulations. These revealed that Nb alloying retarded the stress-induced phase transformation of $\gamma \rightarrow \alpha_2$, favoring a refined microstructure with the dislocation sources from microstructure boundaries and interfaces at high temperature and improving thus the ductility. Our microstructure-informed atomistic models reveal a comprehensive picture of the underlying nanomechanical events.

1. Introduction

Gamma titanium aluminide γ(TiAl)-based intermetallic alloys have various applications as lightweight structural materials due to their properties like low density, good oxidation resistance, high strength and creep resistance at high-temperature [1]. The interesting intermetallic phases for engineering applications are γ-TiAl (ordered face-centered tetragonal, $L1_0$, P4/mmm) and α_2-Ti_3Al (ordered hexagonal, $D0_{19}$, $P6_3/mmc$). The past decades witnessed new generations of γ-TiAl based alloys with increasing service temperatures [1–4]. Among them, TNB (T:TiAl, N: Nb and B: B) and TNM (T: TiAl, N: Nb and M: Mo) alloys [1,2,5,6] made substantial improvements. The stoichiometry of these alloys read: Ti-(42-48)Al-(0-10)X-(0-3)Y-(0-1)Z-(0-0.5)RE where, X = Cr, Mn, Nb, Ta; Y = Mo, W, Hf, Zr; Z = C, B, Si; RE denotes rare earth elements. TNB alloys contain 5–10 at. % Nb and small additions of B and C, whereas TNM alloys have similar concentrations of Nb and Mo [2]. Against this background, Nb plays a crucial role in enhancing the mechanical properties of binary γ(TiAl)-based alloys.

Many experimental works [1,2,7,8] reported that Nb enhances the ductility and strength of TiAl. It reduces the stacking fault energy, favoring the activation of mechanical twins resulting in enhanced strength [7,9] and improved low-temperature ductility [9] of γ(TiAl)-based alloys. The contribution of Nb to increased toughness, tensile strength, and yield strength of γ(TiAl)-based alloys was studied by various experimental works [10–19]. The site preference of Nb on Ti lattice sites was experimentally shown in [20–23]. It is worth emphasizing that the insights from the experimental studies of TiAlNb systems discussed the combined effects of microstructure boundaries and alloying elements, e.g., (Nb, Mo, B, and C) on the TiAl system. [1,2,6,8] reported improvement in mechanical properties of γ(TiAl)-based alloys, e.g., ductility and strength by Nb alloying. Despite several interesting contributions from previous experimental investigations and studies on improving TNB alloys, Nb's isolated contributions to the strength and ductility of these alloys remain unclear. This work aims to address this research question by investigating the effects of Nb on thermo-mechanical behavior of γ(TiAl)-based alloys using atomistic simulations.

Density Functional Theory (DFT) helped to understand the site preference of alloying elements in the γ-TiAl and α_2-Ti_3Al phases [24–28]. Strong site preference of Nb at Ti sites was reported in single phases [24] and in bulk and interface regions [25] in a γ-TiAl/ α_2-Ti_3Al inter-

---

* Corresponding author.
E-mail address: h.ganesan@fz-juelich.de (H. Ganesan).
URL: https://www.hereon.de (H. Ganesan).

[1] Currently at Forschungszentrum Juelich, Germany.

https://doi.org/10.1016/j.matdes.2023.112596
Received 14 October 2023; Received in revised form 27 November 2023; Accepted 18 December 2023

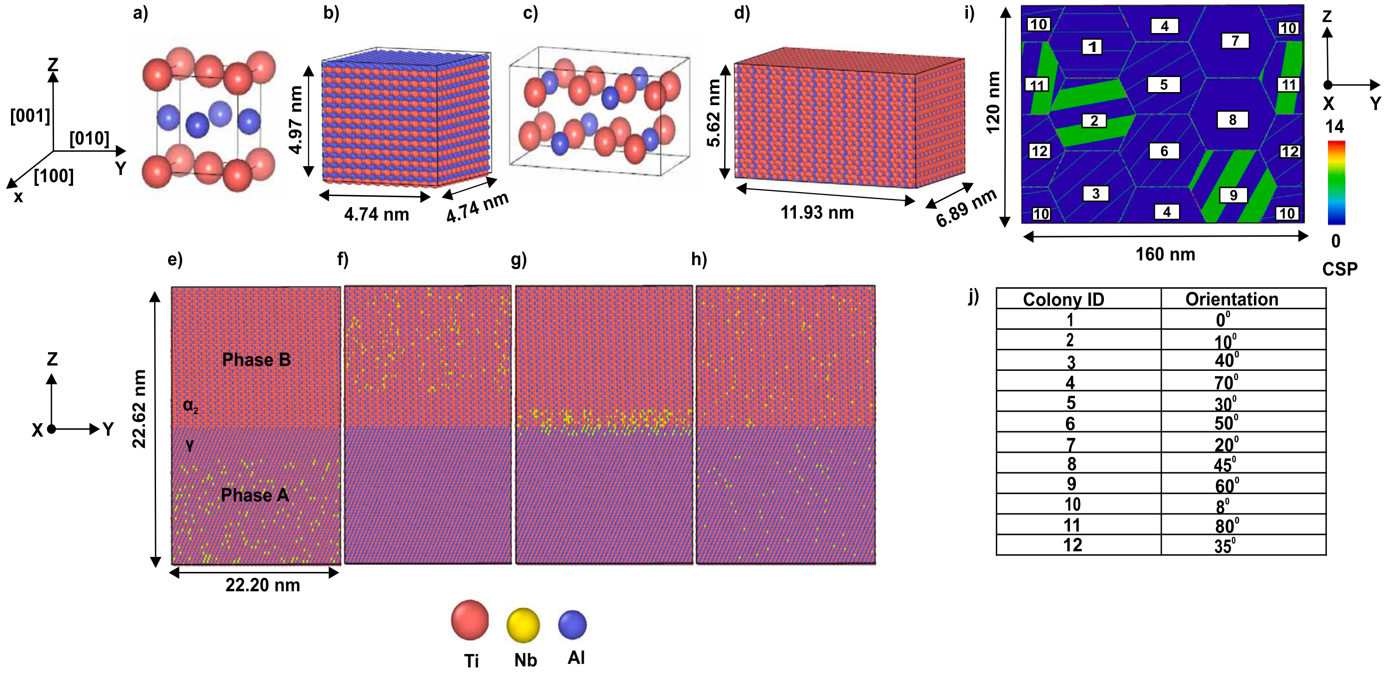

Colony ID	Orientation
1	0°
2	10°
3	40°
4	70°
5	30°
6	50°
7	20°
8	45°
9	60°
10	8°
11	80°
12	35°

Fig. 1. Three categories of atomistic models used in this work: 1) Single phase models ((a) unit cells of γ-TiAl compose (b) γ-TiAl supercell; (c) unit cells of α_2-Ti_3Al compose (d) α_2-Ti_3Al supercell); 2) Single-lamellar interface models (e.g., γ/α_2) with (e) Nb distributed in phase A, (f) Nb distributed in phase B, (g) Nb distributed near lamellar interface, and (h) Nb homogeneously distributed. Phase A corresponds to γ and phase B to α_2, γ_{PT}, γ_{TT} and γ_{RB}; 3) (i) Microstructure-informed atomistic model (MIAM) [40] with 12 nano-colonies, where each colony has different lamella combinations (γ/α_2,γ/γ_{PT},γ/γ_{RB},γ/γ_{TT}), j) Table showing the colony ID (identification number) and orientations of colonies in the MIAM.

face model. The site preference of Nb was also studied using Density of States (DOS) calculation in [26]. However, DFT simulations are prohibitively expensive to investigate atomistic models containing $\geq 10^3$ atoms, thus, preventing us from incorporating complex microstructure features like grain/colony boundaries, interfaces and their contributions.

Molecular dynamics (MD) enables understanding the evolution of many-body atomic systems (routinely 10^3 - 10^9 atoms) besides capturing the interplay between thermal, mechanical, chemical, and microstructure contributions. However, the chemical accuracy and physical reliability of MD simulations are limited by the choice of the underlying interatomic potentials or force fields and appropriate boundary conditions. To gain insight into γ(TiAl)-based alloys, recent MD studies used in particular the Zope potential [29], Farkas binary potential [30], Farkas ternary potential [31], and Kim potential [32]. Recently, [33] developed a new MEAM based Nb-Al-Ti ternary potential which remains to be explored. [34–49] studied TiAl systems using the Zope potential to understand the synthesis of phases, strength, ductility, deformation behavior, fracture mechanism, tensile and creep properties of the material. [50–53] used the Farkas binary potential to investigate point defect formation energy, defect concentration, diffusion mechanisms and nature of crack formation in TiAl systems. Creep mechanisms and self-diffusion in nanocrystalline TiAl alloys were studied in [54,55] using the Kim potential. The Farkas ternary potential was used in [56–59] to investigate high Nb-containing TiAlNb systems to study the B2 phase stability, ductile nature and the diffusion properties of Nb. Previous MD studies [56–61] of TiAlNb did not address the influence of Nb on the thermo-mechanical properties of the material. One major challenge in studying high Nb-containing TiAl phases using MD simulations is the availability of limited interatomic potentials targeting the intermetallic phases of engineering interest.

In this paper, we first assess the transferability of the Farkas potential [31] to different target scenarios and compared it with other established interatomic potentials like the Zope [29] and Kim [32] potentials for γ(TiAl)-based systems. Using the insights obtained this way, we study the isolated effect of Nb atoms on the lattice parameters and neighboring chemical environment using MD simulations and compare them with chemically accurate DFT calculations where possible. Driven by the insights gained, we alter the Nb concentration in atomistic models with varying microstructure complexity to unravel Nb's contributions to the thermo-mechanical behavior of γ(TiAl)-based alloys.

2. Methods

2.1. *Molecular dynamics (MD)*

Intermetallic γ(TiAl)-based alloys of engineering interest consist of two key phases, namely γ-TiAl (ordered face-centered tetragonal $L1_0$ structure) and α_2-Ti_3Al (ordered hexagonal $D0_{19}$ structure). The volume fraction of γ and α_2 depends on the alloy's heat treatments and thermo-mechanical processing [62]. To investigate Nb's contribution comprehensively, we considered three categories of TiAl atomistic models: 1) Single phase models (with and without Nb), 2) Single lamellar interface models (Nb-rich phase/bulk, Nb-rich interface, homogeneously distributed Nb), and 3) Microstructure-informed atomistic models (MIAMs) with nano-polycolonies, as shown in Fig. 1. In the following, we first discuss the interatomic potentials used in these three types of models (section 2.1.1), then their atomistic configuration (sections 2.1.2 - 2.1.4), the different ways we resembled alloying in them (section 2.1.5) and we mimicked tension tests with them (section 2.1.6) and how they were implemented computationally (section 2.1.7).

2.1.1. *Interatomic potentials*

Herein, we primarily used the ternary Farkas potential [31] to define the interatomic interactions of the TiAlNb system. To realize this potential, the developers combined three binary potentials, namely one for Nb-Al (fitted for A15 Nb_3Al and DO_{22} $NbAl_3$), one for Nb-Ti (for disordered BCC phase), and one for Ti-Al [30]. The resulting ternary potential (NbTiAl) was reported to predict the Nb-rich phases like the orthorhombic Ti_2AlNb and ternary B_2 phase. The Farkas potential [31] was used to study and predict the behavior of the ternary TiAlNb system [57], although no input pertaining to the ternary system was included in the fitting procedure of this potential. We examined also other secondary interatomic potentials, namely the Zope potential [29], Kim potential [32], and Xiang potential [33] for the TiAl system to investigate the scope and transferability of the Farkas potential. Among them, the Zope potential and Kim potential were extensively used previously [34–41], to study several aspects in binary γ-TiAl systems. Most recently, Xiang et al. developed an interatomic potential for the TiAlNb system [33]. A systematic investigation of this new ternary potential is beyond the scope of this work. Therefore, this potential was used only for selected models (for more information, see A). For brevity, in this article, we refer Farkas ternary potential [31] as Farkas potential (otherwise as Farkas binary potential [30] explicitly).

2.1.2. Single phase models

The single-phase models of γ-TiAl ($a = 3.950$ Å, $c/a = 1.048$) and α_2-Ti_3Al ($a = 5.740$ Å, $c/a = 0.815$) were modeled with the Farkas binary potential [30], where such single phases represent the lamellae of the constituent intermetallic phase. The single-phase γ-TiAl and α_2-Ti_3Al models were realized with simulation box dimensions of 4.74 nm × 4.74 nm × 4.97 nm and 6.89 nm × 11.93 nm × 5.62 nm, respectively. Both of them were modeled with crystallographic orientation of X-direction [1 0 0], Y-direction [0 1 0], and Z-direction [0 0 1]. These single-phase models aid in understanding the transferability of Farkas potential [31] by comparing it with the Zope and Kim potentials. We computed the formation energy (ΔE_f) of point defects, elastic constants, and cohesive energy (E_{coh}) at $T = 0\,K$ as the Farkas potential was fitted to predict some of these properties. Furthermore, we computed the phase transition temperature to evaluate the Farkas potential's predictive abilities at elevated temperatures (2400 K). Some tension tests were performed at ground state and room temperature to assess the mechanical property predictions.

2.1.3. Interface models

We realized atomistic single-lamellar interface models of γ/α_2 and three γ/γ variants (i.e., γ/γ_{PT}, γ/γ_{RB}, and γ/γ_{TT}, realized by a rotation around the $<111>_\gamma$ axis by 60°, 120° and 180°, resulting in a pseudo twin (γ_{PT}), rotational boundary (γ_{RB}) and true twin (γ_{TT})) with box dimension of 22.6 nm × 22.2 nm × 22.4 nm, containing 675,840 atoms. Here, γ-TiAl was modeled with the crystallographic orientations of X-direction [1–1 0], Y-direction [1 1–2], and Z-direction [1 1 1]. Similarly, we modeled α_2-Ti_3Al with X-direction [1–1 0], Y-direction [1 1 0], and Z-direction [0 0 1]. The single-lamellar interface models comprised two phases, namely A and B in Fig. 1e - h. Phase A denotes γ-TiAl, phase B denotes either α_2-Ti_3Al or one of the three variants ($\gamma_{PT}, \gamma_{RB}, \gamma_{TT}$). Phase A and phase B represent one of the possible constituent intermetallic phases of the target microstructure, respectively. Furthermore, we alloyed the above atomistic models with different Nb concentrations (1.0 at.%, 2.0 at.%, 5.0 at.%, 6.5 at.%, and 7.5 at.%) to understand the relation between Nb, microstructure features (e.g., interfaces/boundaries) and thermo-mechanical properties at high temperatures (e.g., 700 K, 900 K).

2.1.4. Microstructure-informed atomistic models

We considered microstructure-informed atomistic models (MIAMs) as introduced previously in [40]. They consisted of 12 nano-sized colonies in a periodic domain of the size 12 nm (X) × 160 nm (Y) × 120 nm (Z), containing 14,612,466 atoms. Each colony comprises several of one of the following four interfaces: γ/α_2, γ/γ_{PT}, γ/γ_{RB}, and γ/γ_{TT}. The MIAMs used the experimentally informed microstructure parameters like lamella thickness (λ^γ, λ^{α_2}), α_2 volume fraction (φ^{α_2}), and distance between subsequent α_2 lamellae (d^{α_2}) reported already in our previous work [40]. The orientation of each colony (designated with a colony ID) around the X-axis is provided in Fig. 1 (i, j), along with the centrosymmetry parameter (CSP) values. The CSP measures the local lattice distortion of an atom, thus, aiding in characterizing defects, interfaces, and colony boundaries in the MIAM. We considered the Nb concentrations 0.0 at.%, 0.5 at.%, and 1.0 at.% at temperatures 300 K, 500 K, 700 K and 900 K.

2.1.5. Alloying

Many experimental studies [21,22] along with several other works [24–26,59,63] show Nb atoms prefer Ti sites in γ(TiAl)-based alloys. Our DFT calculations yielded similar site preferences of Nb at Ti sites (see section 2.2). Therefore, we realized the ternary atomistic models by substituting Nb atoms at Ti sites to achieve different target Nb concentrations. e.g., 0.0 - 5.0 at.% with 1.0 at.% increments in the single-phase models. Similarly, in the single-lamellar interface models, Nb was introduced at random Ti sites either in Phase A or Phase B regions (Nb-rich phase), interface regions (Nb-rich interface) or homogeneously everywhere (Fig. 1 e - h) to reach target concentrations of 1.0 at.%, 2.0 at.%, 5.0 at.%, 6.5 at.%, and 7.5 at.%, respectively. Based on our preliminary investigation of the Farkas potential for different microstructures, we studied the transferability limits of this potential to microstructure models with complex interfaces. The transferability limit of an interatomic potential refers to the extent to which the potential can reasonably describe the material system's behavior beyond those for which it was originally parameterized. Thus, in our MIAM models, we considered only low Nb concentrations (0.5 at.% Nb and 1.0 at.% Nb), wherein Nb atoms were introduced at a distance of at least 4 nm from the grain boundaries. We also reached the transferability limit of the Farkas' potential for Nb concentrations above 2 at.% near the single lamellar interface models for Nb-rich interfaces, see Fig. 1). Note the observed transferability limits are valid only for the assumption that Nb atoms occupy Ti sites in our atomistic models.

2.1.6. Simulated tension tests

To simulate tension tests, we applied in our MD models uniaxial tension loading along the Z-direction at a strain rate of 10^9/s, with periodic boundary conditions in all directions. To this end, we used single phase models of γ-TiAl and α_2-Ti_3Al, single-lamellar interface models, and MIAM models both with and without Nb to understand Nb's influence on the high-temperature deformation behavior of TiAl-based alloys.

First, we performed a free energy minimization of the atomistic models using a combination of conjugate gradient (CG) and FIRE algorithms in LAMMPS. Then, we equilibrated the models for temperature (1 K) and pressure (1 bar) using NVT and NPT for 100 ps each. Later, the simulation models were heated to the target temperature of 300 K for single phase models, 700 K and 900 K for interface models, and 300 K, 500 K, 700 K and 900 K for MIAMs. Note that the defect-free single-phase models were considered only for the ground state (to enable comparisons with DFT) and room temperature where possible. The heating rate for all the considered models was 3 K/ps followed by thermal equilibration for 100 ps. The timestep size was 1 fs for models without Nb using the Zope, Farkas, and Kim potentials) and 0.1 fs for models with Nb using the Farkas' potential.

2.1.7. Implementation

The MD simulations were realized using the classical MD code Large-scale Atomic/Molecular Massively Parallel Simulator (LAMMPS) [64]. We used some in-house tools, along with Atomsk [65] and VESTA, for constructing the atomistic models used in this work (Fig. 1). We used OVITO [66] for visualization.

2.2. Density functional theory (DFT)

We performed some Density Functional Theory (DFT) calculations using Quantum Espresso [67] to assess the chemical accuracy of the

Table 1

TiAl material parameters computed with the interatomic potentials of Farkas [31], Zope [29], and Kim [32]. C_{11}-C_{66} denote the entries of the material stiffness matrix (Voigt convention) for characterizing elastic constants, ΔE_f V_{Ti} and ΔE_f V_{Al} denote raw formation energy of Ti and Al vacancies, ΔE_f Al_{Ti} and ΔE_f Ti_{Al} denote raw formation energy of Al and Ti antisites, and E_{coh} denotes the cohesive energy, respectively. Elastic constants (C_{11}-C_{66}) are given in GPa, whereas raw formation energies and cohesive energy are given in eV.

Quantities	γ-TiAl			α_2-Ti_3Al		
	Farkas	Zope	Kim	Farkas	Zope	Kim
C_{11}	245.50	196.67	181.11	233.60	199.96	200.58
C_{33}	352.02	212.79	234.39	285.27	224.51	238.92
C_{12}	116.24	107.49	76.27	109.27	88.51	107.78
C_{13}	190.85	113.53	133.75	87.58	74.43	91.17
C_{44}	146.02	92.06	86.00	57.77	51.42	45.56
C_{66}	71.58	85.16	61.56	62.21	56.04	46.44
ΔE_f V_{Ti}	-6.50	-6.81	-6.60	-6.28	-6.73	-6.60
ΔE_f V_{Al}	-5.21	-5.37	-5.32	-5.86	-6.07	-5.81
ΔE_f Al_{Ti}	-1.97	-1.84	-1.67	-1.23	-1.03	-1.10
ΔE_f Ti_{Al}	0.97	1.08	0.90	0.56	0.37	-0.056
E_{coh}	-4.40	-4.51	-4.50	-4.68	-4.77	-4.78

Farkas' potential [31] for the target intermetallic phases at the ground state. The electron-ion interactions were described using projected augmented wave (PAW) [68] potentials. Exchange and correlation effects were treated within the generalized gradient approximation (GGA) using the Perdew–Burke–Ernzerhof (PBE) [69] functional. We considered a plane wave cut-off energy of 400 eV with the electronic energy and atomic force components converged within 10^{-6} eV and 0.01 eV/Å, respectively. The simulation supercells represent the single intermetallic phases, i.e., γ-TiAl (ordered face-centered tetragonal $L1_0$) and α_2-Ti_3Al (ordered hexagonal $D0_{19}$) consisting of 32 atoms, whose unit cell representation is provided in Fig. 1 a, c. The Brillouin zone of the supercell was sampled using a 7×7×7 Monkhorst-Pack [70] k-point mesh. We computed formation energy, electron localization function (ELF), and partial density of states (PDOS) by substituting an Nb atom at either Ti or Al lattice sites.

Several previous works [24–26,59,63,71] claimed a Nb preference of Ti sites. To verify this claim, we computed Nb's site preference, by substituting the Nb atom either at Ti or Al sites, following [24] and using

$$E_f^{Ti} = \frac{E^{\eta}_{Ti_{m-1}NbAl_n} - [(m-1)E_{Ti} + E_{Al} + E_{Nb} + nE_{Al}]}{m+n} \tag{1}$$

and

$$E_f^{Al} = \frac{E^{\eta}_{Ti_m NbAl_{n-1}} - [mE_{Ti} + E_{Al} + E_{Nb} + (n-1)E_{Al}]}{m+n} \tag{2}$$

Equations (1) and (2) refer to the formation energy of a TiAl atomic configuration with Nb atoms substituted either at Ti or Al sites, respectively. $E^{\eta}_{Ti_{m-1}NbAl_n}$ and $E^{\eta}_{Ti_m NbAl_{n-1}}$ denote the total energy of the supercell configuration describing the intermetallic phase η (i.e., γ-TiAl and α_2-Ti_3Al), where one Nb atom replaces a single Ti or Al atom. E_{Al}, E_{Ti}, and E_{Nb} are the total energies of Al in FCC (face-centered cubic), Ti in HCP (hexagonal close-packed) and Nb in SC (simple cubic) structures, respectively.

Using DFT calculations for TiAl systems, we investigated Nb's site preference and Nb's chemical interactions with host atoms in γ-TiAl and α_2-Ti_3Al. To this end, we computed the electron localization function (ELF), which measures the probability of finding an electron in the neighborhood of a reference electron with the same spin [72].

3. Results and discussion

3.1. Assessment of Farkas' interatomic potential

3.1.1. Binary TiAl systems

Herein, we evaluate the predictive ability of the Farkas [31] potential against the one of the Zope [29] and Kim [32] potential for the target intermetallic phases, i.e., γ-TiAl and α_2-Ti_3Al in TiAl system. Table 1 provides computed values of elastic constants, formation energy (ΔE_f), and cohesive energy (E_{coh}) of point defects for the different interatomic potentials considered. We also calculated the phase transition temperature of the intermetallic phases of interest. To evaluate the mechanical property prediction, we compared the Ultimate Tensile Strength (UTS) of intermetallic phases, i.e., γ-TiAl and α_2-Ti_3Al.

Farkas potential [31] predicts slightly higher elastic constants compared to the Zope [29] and Kim potential [32]. Such discrepancy could stem from two aspects: first, the three interatomic potentials relied on different DFT and experimental data; second, Farkas' potential was targeted for ternary intermetallic regions, e.g., orthorhombic Ti_2AlNb with high Nb content.

Although the high elastic constants for the γ phase (at T = 0 K, refer Table 1) from Farkas potential can influence the reversible deformation behavior, those effects could be less pronounced in atomistic models (e.g., MIAMs) with high microstructure complexity encompassing phase fractions, lamellar thicknesses, lamellar interfaces, and colony boundaries. Considering the temperature and directional dependence of elastic constants, the interplay of temperature, strain rate, and microstructure complexity (i.e., phase volume fractions and their crystallographic directions) determine the thermo-mechanical behavior of TiAl alloys. Furthermore, we calculated the formation energy (ΔE_f) of four point defects, namely Ti vacancy (V_{Ti}), Al vacancy (V_{Al}), antisite at Ti sublattice (Al_{Ti}), and antisite at Al sublattice (Ti_{Al}). Our computations suggest that Ti vacancy (V_{Ti}) and antisite at Ti sublattice (Al_{Ti}) are preferred energetically over Al vacancy (V_{Al}) and antisite at Al sublattice (Ti_{Al}) in both γ-TiAl and α_2-Ti_3Al. To this end, vacancy and antisite formation mechanisms might act as precursors for the diffusion of alloying elements in γ-TiAl and α_2-Ti_3Al, preferably at Ti sites. Thus, a critical point defect concentration in the system is foreseen to favor diffusion. In general, the values of the cohesive energy E_{coh} and the energy of ΔE_f for point defects agreed reasonably well between the three potentials of Farkas, Zope and Kim. This suggests a generally good transferability of Farkas potential also for binary intermetallic phases, i.e., γ-TiAl and α_2-Ti_3Al.

To evaluate the ability of Farkas' [31] potential to predict melting points and phase transitions, the single intermetallic phase models (i.e., α_2-Ti_3Al and γ-TiAl) were heated to 2400 K at a heating rate of 2 K/ps. The models showed phase transitions around 1774 K (α_2-Ti_3Al) and 2055 K (γ-TiAl), respectively (Fig. 2). Compared to Farkas' potential, the other two potentials predicted higher transition temperatures for both phases (Zope potential: 2181 K (α_2-Ti_3Al) and 2053 K (γ-TiAl), Kim potential: 2712 K (α_2-Ti_3Al), 2475 K (γ-TiAl)). Note that the experimentally [1,73] reported melting points of 1473 K for α_2-Ti_3Al and 1723 K for γ-TiAl are much closer to the prediction based on Farkas' potential compared to the other two potentials. These experimental ob-

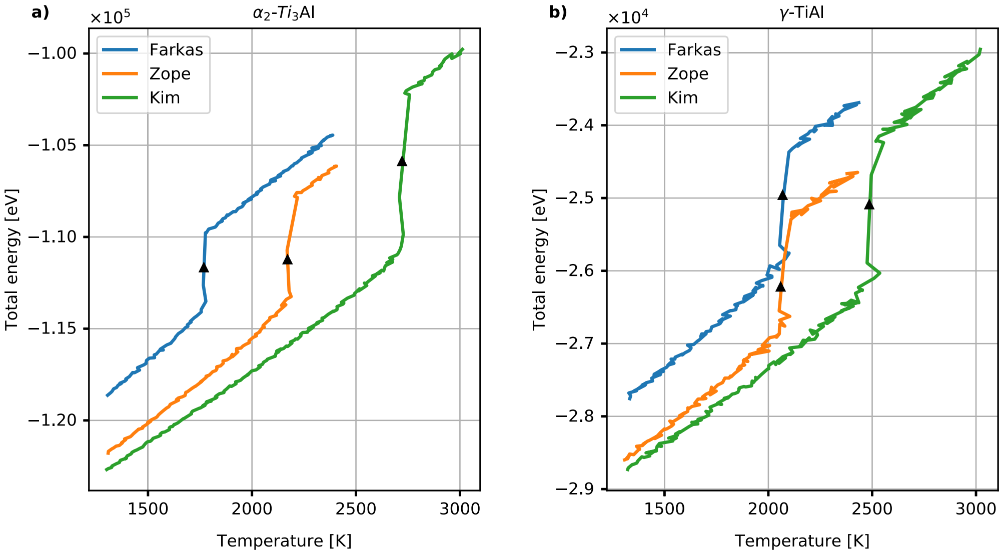

Fig. 2. Comparison of heating curves for single phases of (a) α_2-Ti$_3$Al and (b) γ-TiAl using the interatomic potentials of Farkas [31], Zope [29] and Kim [32]. The black markers denote the phase transition region for each intermetallic phase.

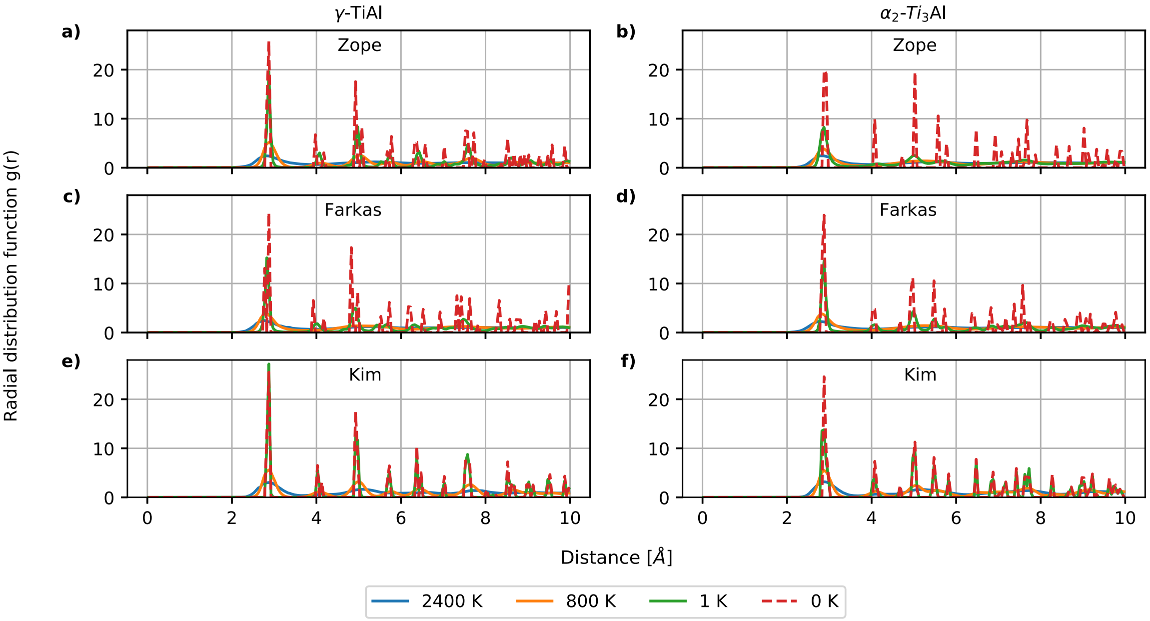

Fig. 3. Radial distribution function g(r) for γ-TiAl (left) and α_2-Ti$_3$Al (right) and the potentials of Zope [29] (top), Farkas [31] (middle), and Kim [32] (bottom) at temperatures 2400 K, 800 K, 1 K, and 0 K (ground state for comparison) to demonstrate the ability of interatomic potentials to sample the phase transition.

servations agree with [74], reporting that γ-TiAl precipitated or formed either from α_2-Ti$_3$Al or α-Ti, underlining that the α_2-Ti$_3$Al phase has a lower melting point than the γ-TiAl phase. While this is in agreement with the computations based on Farkas' potential, the potentials of Kim and Zope predict an inverse order of the melting points.

After simulating heating, we simulated also cooling to evaluate the capability of Farkas' potential to capture phase transformation. We cooled the configurations from 2400 K to 1 K at a general cooling rate of 2 K/ps and a cooling rate of 0.01 K/ps specifically for γ-TiAl because in agreement with [75] we observed difficulties in generating an ordered intermetallic phase at higher cooling rates. Fig. 3 shows the radial distribution function (RDF) for γ-TiAl and α_2-Ti$_3$Al for selected temperatures (0 K (ground state), 1 K, 800 K, 2400 K). The agreement between the peaks at low temperatures (0 K, 1 K) for the three different potentials of Farkas, Zope and Kim underlines the ability of Farkas' potential to capture the same effects as Zope's potential though at a much higher cooling rate, i.e., 2 K/ps.

We simulated tension tests to evaluate how different potentials predict the mechanical behavior of the TiAl system. To this end, we applied a strain rate of 10^9/s on single phase models of γ-TiAl and α_2-Ti$_3$Al equilibrated at 300 K. The corresponding stress-strain curves of the tension tests are plotted in Fig. 4. For γ-TiAl, the Farkas and Zope potentials yield similar UTS, while the Kim potential showed a slightly higher value. For α_2-Ti$_3$Al, the Kim and Zope potential yield a similar UTS, the Farkas potential a significantly lower one. Note that Farkas' potential yields a lower strength for α_2-Ti$_3$Al than for γ-TiAl (although along the [0 0 1] direction), which will be crucial in interpreting the results of the complex models below. Fig. 5 shows the dislocation density evolution of single phase γ-TiAl and α_2-Ti$_3$Al during simulated tensile tests, using DXA analysis [66]. For γ-TiAl, both the Farkas and Zope

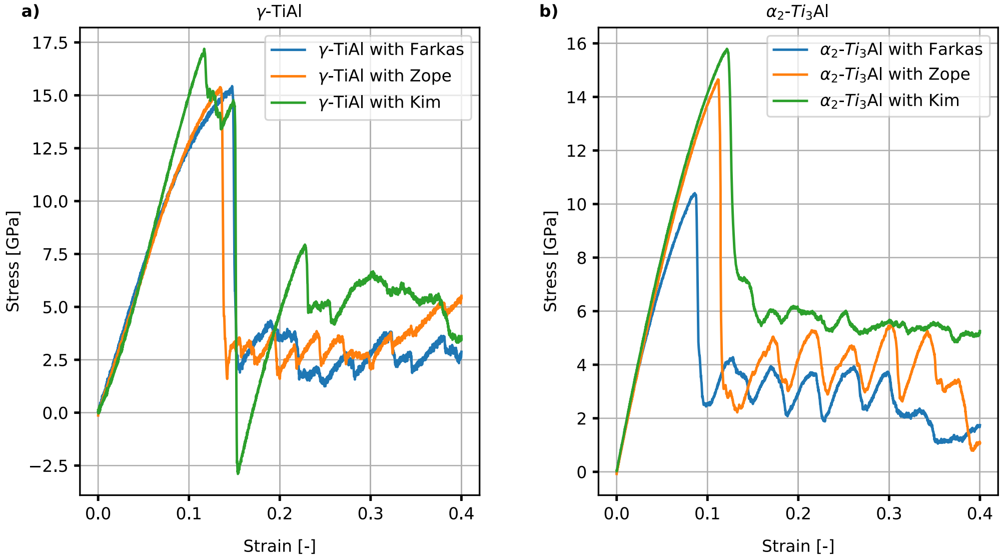

Fig. 4. Stress-strain curves in simulated tensile tests at 300 K with a strain rate of 10^9/s for a) γ-TiAl and b) α_2-Ti$_3$Al using the three different interatomic potentials of Farkas [31], Zope [29], and Kim [32].

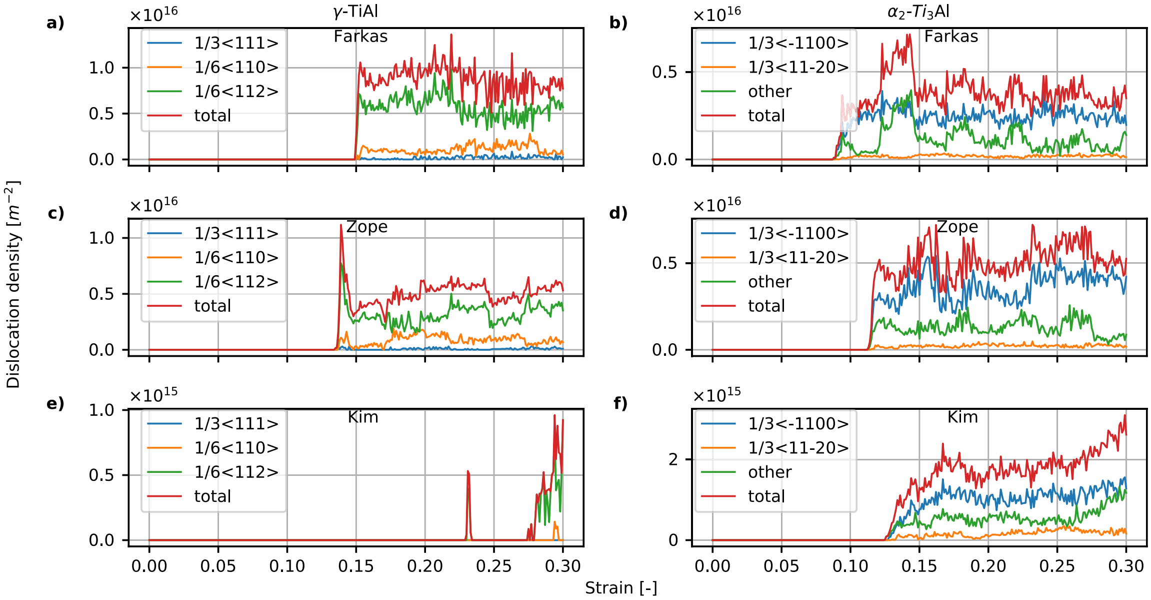

Fig. 5. Dislocation density in simulations of tension tests using MD for the three different interatomic potentials of Farkas [31], Zope [29], and Kim [32].

potential showed qualitatively similar dislocation densities (Fig. 5 a, c), whereas the Kim potential delayed the onset of dislocations (Fig. 5 e). For α_2-Ti$_3$Al, again only minor differences in the dislocation evolution are observed between the Farkas and Zope potential, whereas the Kim potential leads to a remarkably late onset of dislocation formation but at the same time considerably higher overall densities for higher strains. These observations agree with [76], where dislocation densities between simulations with the Zope and Kim potential were compared. We attribute the deviations of the results obtained with the Kim potential compared to the other two potentials to its underlying MEAM (Modified Embedded Atom Method) formulation, which systematically accounts for the angular contributions.

Herein, we evaluated the transferability of the Farkas potential in predicting the behavior of single intermetallic phases, i.e., γ-TiAl and α_2-Ti$_3$Al, by comparing it with the Zope and Kim potential.

In summary, our computations provided elastic constants, point defect formation energies, cohesive energies, transition temperature, and predictions of the mechanical behavior. The critical analysis of our results indicates that the ternary Farkas potential is applicable (i.e., transferrable) also to binary intermetallic phases (i.e., γ-TiAl and α_2-Ti$_3$Al) that are of engineering interest. That is, it can also be used in Nb-free atomistic models in the forthcoming subsections.

3.1.2. *Effect of Nb in intermetallic phases*

We performed DFT calculations to investigate how Nb influences lattice constants, site preference (energetics), and electron localization functions of neighboring Ti and Al atoms in single intermetallic γ-TiAl and α_2-Ti$_3$Al. These DFT calculations served as a reference point to evaluate the ability of Farkas' potential [31] to capture the effects of Nb in γ-TiAl and α_2-Ti$_3$Al phases. The existing claim of Nb preference of Ti sites [24–26,59,63,71] was verified by our DFT calculations, which helped us to construct microstructure-informed atomistic models. Analyzing the electron localization function (ELF) and the partial density of states (PDOS) sheds light on the atomic interactions and chemistry of the bonding in the neighborhood of Nb atoms.

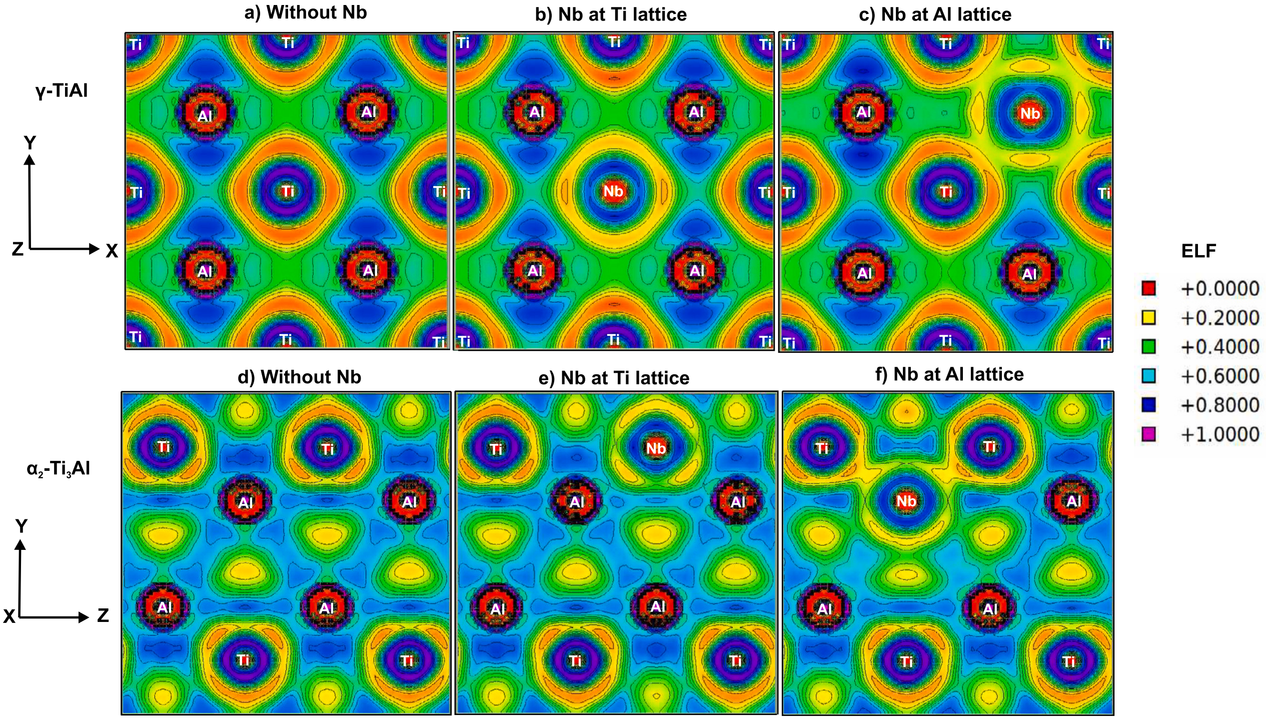

Fig. 6. Comparison of electron localization function (ELF) using DFT: γ-TiAl (top) and α_2-Ti$_3$Al (bottom) before and after introducing an Nb atom either at Ti or Al site.

For the γ-TiAl phase, the formation energies (E_f^{Ti}) were computed as -1.5697 eV (Nb placed at Ti site) and -0.7908 eV (Nb placed at Al site), respectively. Similarly, for α_2-Ti$_3$Al the computed formation energies were -0.7919 eV (Nb placed at Ti site) and -0.5915 eV (Nb atom placed at Al site). Herein, for both intermetallic phases, Nb at the Ti site had a lower formation energy, i.e., was energetically preferred. Hence, we placed Nb atoms at the Ti lattice sites in our atomistic models.

Fig. 6 shows the ELF for γ-TiAl and α_2-Ti$_3$Al when a Nb atom is placed at a Ti and Al sites, respectively. The ELF measures the probability of finding an electron in the neighborhood of a reference electron with the same spin [72]. The bonding interaction is considered metallic if ELF ≤ 0.5 and covalent if ELF > 0.5. Fig. 6a shows that in the region between Ti and Al atoms ELF > 0.5, suggesting a Ti(3d)-Al(3p) covalent bond. Similarly, the region between Ti and Ti atoms exhibits covalent Ti(3d)-Ti(3d) bonds. In γ(TiAl)-based alloys, Ti(3d)-Al(3p) covalent bonds with strong direction sensitivity are shown to increase the shear strength [77,78]. The ductility of γ(TiAl)-based alloys can be improved by adding alloying elements (Nb, Be, Si, V, Cr, Mn, Fe, Co, Ni, Zr, Mo) which in turn reduce the Ti(3d)-Al(3p) bonding or increases the Ti(3d)-Ti(3d) bonding [77,79]. In contrast to Fig. 6a, no significant changes are observed in Fig. 6b for electron localization in the vicinity of Nb atoms. However, Fig. 6c shows strong electron localization between Nb and neighboring Ti and Al atoms due to enhanced Nb(d)-Ti(d) and Nb(d)-Al(p) bonds. Similarly, for α_2-Ti$_3$Al (Fig. 6d-f), Nb at Al sites shows strong electron localization (Fig. 6f) with the neighboring Al and Ti atoms due to the strengthening of Nb(d)-Ti(d) and Nb(d)-Al(p) bonds. Our observation agrees very well with [77], which reported that the addition of 4d transition elements (X) in TiAl systems strengthens both the X(d)-Ti(d) and X(d)-Al(p) bonds.

Figs. 7 and 8 show the PDOS (partial density of states) of γ-TiAl and α_2-Ti$_3$Al, when a Nb atom is placed at a Ti and Al lattice site, respectively. Both show the existence of bond interactions between Ti(3d)-Al(3p) as their PDOS peaks at similar energy values. For γ-TiAl, Nb atoms reduce the electron density of Al(3p) electrons, whereas for α_2-Ti$_3$Al the reduction is slightly more pronounced. Such reduction weakens Ti(3d)-Al(3p) interactions due to Nb explaining possibly the increased ductility in γ-TiAl and α_2-Ti$_3$Al. Fig. 7 shows a higher peak of the local density of 4d electrons of Nb atoms when placed at the Ti sites rather than Al sites in γ-TiAl, whereas the density is similar for α_2-Ti$_3$Al. Our observation agrees with [26], which reported more 4d electrons of Nb to participate in the bond formation in γ-TiAl, thus, showing the site preference of Nb at Ti sites over Al sites.

Besides DFT calculations, we performed also MD simulations to study the effect of Nb atoms on the thermo-mechanical behavior of the target intermetallic phases. To this end, we investigated the effects of varying Nb concentrations (i.e., 0.0 - 5.0 at.%) on the lattice constants of γ-TiAl and α_2-Ti$_3$Al. For γ-TiAl, Nb atoms at Ti sites increase the lattice constant ‘a’ but decrease ‘c’ (Fig. 18a in the appendix). This observation agrees with other previous works [8,59,71]. By contrast, for α_2-Ti$_3$Al, our simulations showed negligible changes of the lattice constant ‘a’ but decreased ‘c’ due to Nb alloying (Fig. 18b in the appendix).

Fig. 9b (γ-TiAl) and 9d (α_2-Ti$_3$Al) show computed displacements for selected Ti and Al atoms in the neighborhood of an Nb atom. For γ-TiAl, Ti and Al atoms move away from and towards Nb atoms, respectively, along the X and Y directions (Fig. 9). Along the Z direction, they move towards the Nb atoms. Note that the computed atomic displacements of neighboring Ti and Al atoms are in agreement with the previously discussed increase in the lattice constant ‘a’ and decrease in the lattice constant ‘c’ as shown in Fig. 18a. For α_2-Ti$_3$Al, such direction-specific displacements could not be clearly distinguished since the neighboring Al and Ti atoms showed collective displacements (Fig. 9d), which explains the unchanged lattice constant ‘a’ observed in Fig. 18b.

Next, we simulated tension tests of single intermetallic phase models (models b, d in Fig. 1) using MD simulations at finite temperatures with varying Nb concentrations (0.0 - 5.0 at.%) to understand the effect of Nb on thermo-mechanical deformation behavior. The resulting stress-strain curves are plotted in Fig. 10 and Table 2 shows the computed UTS values. The enhanced fluctuations in the stress-strain curves for single phase γ-TiAl and α_2-Ti$_3$Al may be attributed to pressure fluctuations resulting from lattice distortions due to high Nb alloying. Furthermore, it is worth mentioning that Farkas’ ternary interatomic potential was originally developed for Nb-rich phases as host systems, whereas the

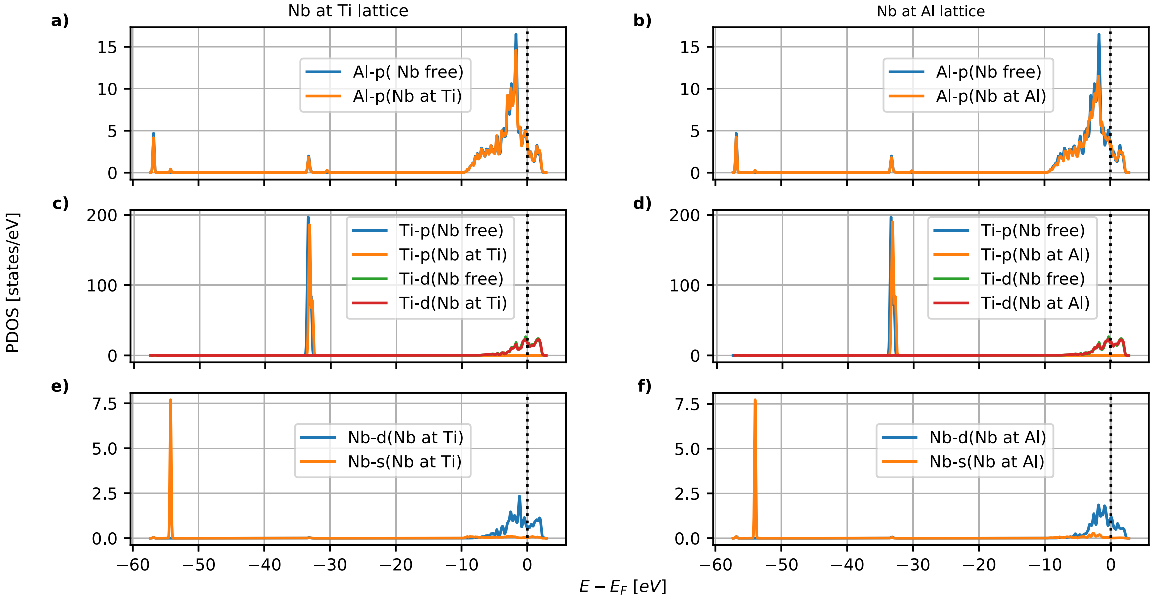

Fig. 7. Partial density of states (PDOS) of γ- TiAl with Nb at Ti site (left) and Nb at Al site (right) and PDOS of Al-p orbitals (top), Ti-p and Ti-d orbitals (middle) and Nb-d and Nb-s orbitals (bottom). The black dotted lines depicts the Fermi energy level.

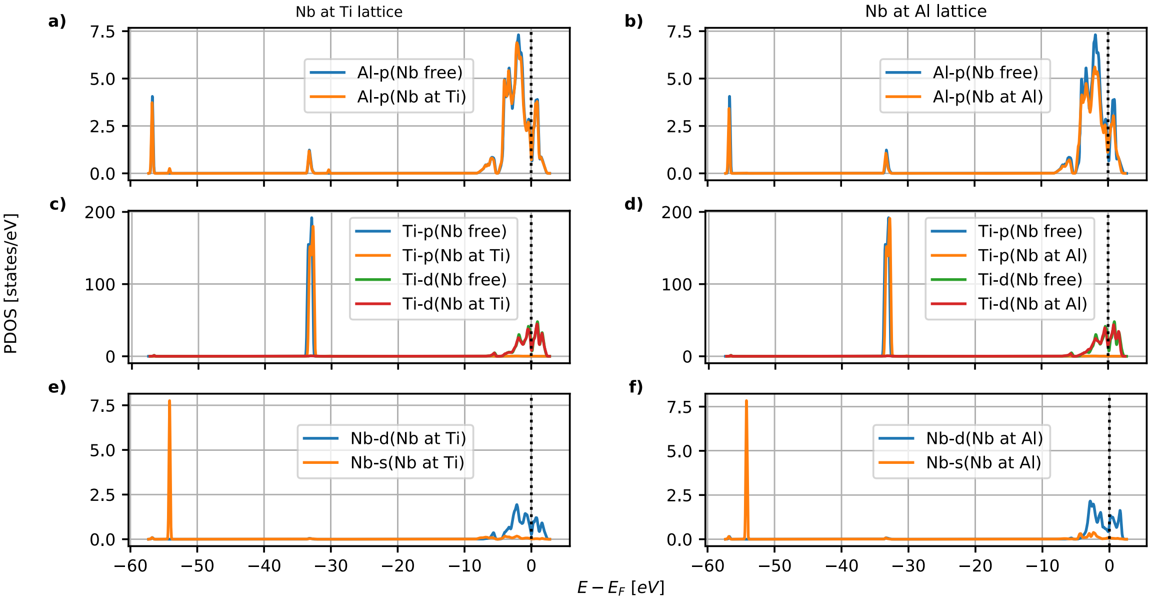

Fig. 8. Partial density of states (PDOS) of α_2-Ti_3Al with Nb at Ti site (left) and Nb at Al site (right) and PDOS of Al-p orbitals (top), Ti-p and Ti-d orbitals (middle) and Nb-d and Nb-s orbitals (bottom). The black dotted lines depict the Fermi energy level.

Table 2
Computed ultimate tensile strength (UTS) of single phase γ-TiAl and α_2-Ti_3Al with increasing Nb concentration.

Nb conc [at.%]	UTS of γ-TiAl [GPa]	UTS of α_2-Ti_3Al [GPa]
0.0	15.33	10.39
1.0	11.76	8.19
2.0	10.69	7.04
3.0	10.26	6.14
4.0	10.29	5.30
5.0	9.69	4.42

current configurations are different from the intended target scenarios based on our preliminary studies. We observed that the UTS values of single phase γ-TiAl and α_2-Ti_3Al decrease with Nb content (Table 2 and Fig. 10). Note that this observation requires careful interpretation because the simple single intermetallic phase models considered here were oriented in primitive orientations and were devoid of other complex features such as grain boundaries and secondary alloying elements.

In this subsection, our investigation yielded several interesting aspects of Nb in both γ-TiAl and α_2-Ti_3Al. We evaluated the site preference using DFT, showing that Nb atoms prefer Ti lattice sites over Al sites. The ELF revealed the bonding of Nb to neighboring atoms in both γ-TiAl and α_2-Ti_3Al. The PDOS plots (Fig. 7 and 8) provided a possible explanation for the enhanced ductility of γ-TiAl and α_2-Ti_3Al resulting from Nb addition the weakening of Ti(3d)-Al(3p) interactions. Our MD simulations of single phase γ-TiAl and α_2-Ti_3Al also aid in understanding the effect of Nb alloying (0.0 – 5.0 at.%) on lattice constants. Accordingly, in γ-TiAl, the lattice constants ‘a’ increased and ‘c’ decreased with Nb, whereas for α_2-Ti_3Al, ‘a’ re-

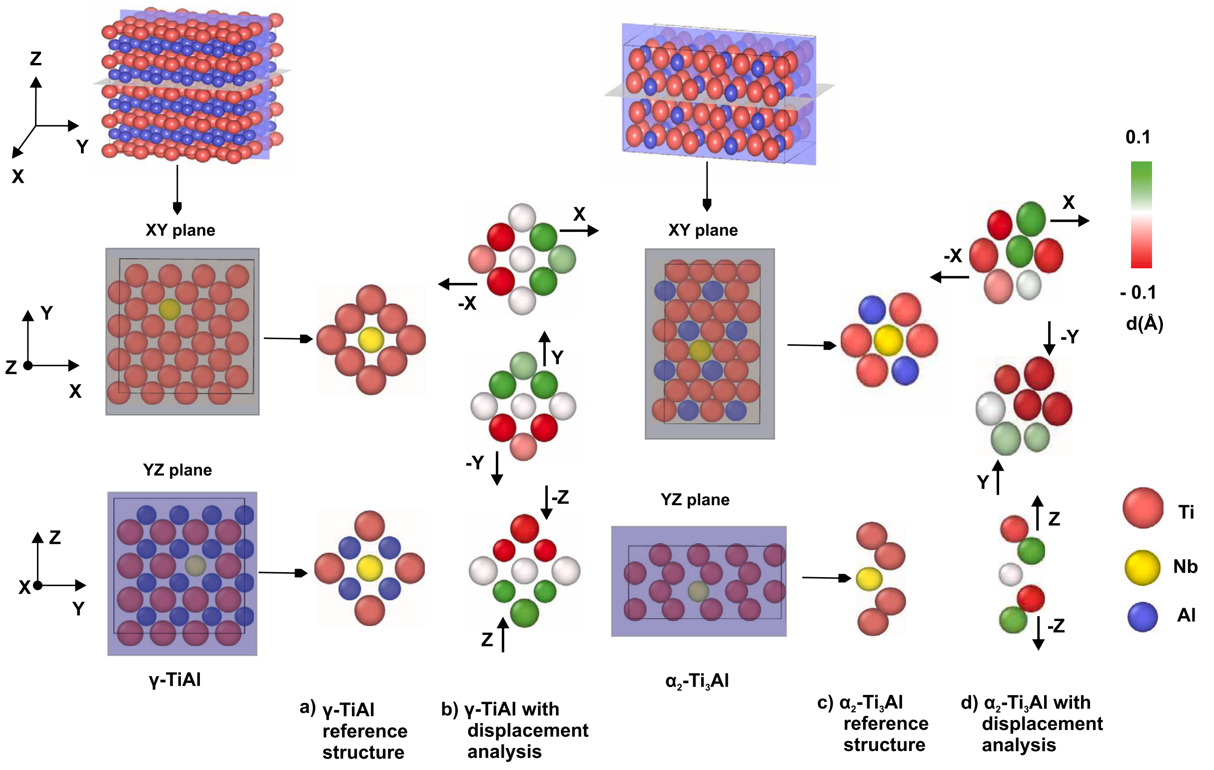

Fig. 9. Displacement profile of the atomic neighborhood in γ-TiAl and α_2-Ti$_3$Al resulting from Nb introduction. Herein, a) and c) correspond to the reference structure of γ-TiAl and α_2-Ti$_3$Al, whereas b) and d) denote the respective phases with displacement analysis. The atoms are color-coded as per their chemical types (Ti, Al, Nb), except for the displacement analysis (b, d), where the atoms are color-coded with their displacement (color bar).

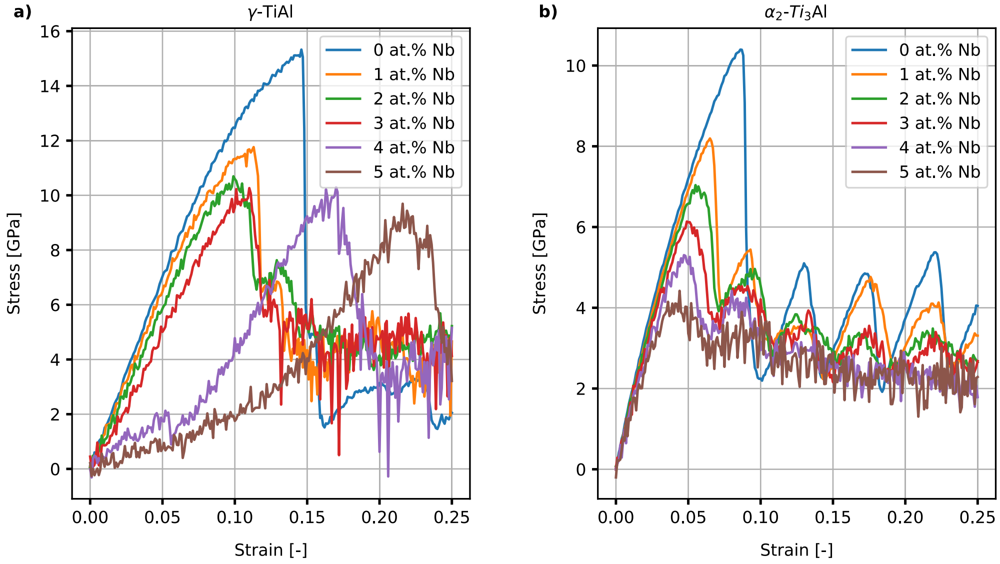

Fig. 10. Stress-strain curves for a) γ-TiAl and b) B) α_2-Ti$_3$Al in simulated tension tests at room temperature with a strain rate of 10^9/s using Farkas' [31] potential for different Nb concentrations (0.0 at.%, 1.0 at.%, 2.0 at.%, 3.0 at.%, 4.0 at.%, and 5.0 at.%).

mained nearly constant, but 'c' decreased. The displacement analysis of Nb's neighboring Ti and Al atoms in Fig. 9 underpins these observed changes. Understanding how the introduction of Nb affects lattice constants provides insights into the potential lattice distortions that may arise in simulations involving complicated models containing Nb. Our DFT calculations and atomistic MD simulations have contributed to a deeper comprehension of the site preference of Nb atoms, their influence on the lattice parameters, and their contribution to improved ductility in TiAl systems. These findings are poised to play a crucial role in deciphering the intricate alterations induced by Nb addition within the upcoming complex atomistic models.

3.2. Thermo-mechanical behavior of TiAlNb

In this subsection, we aim to investigate the thermo-mechanical behavior of single-lamellar interfaces and more realistic MIAMs alloyed with Nb.

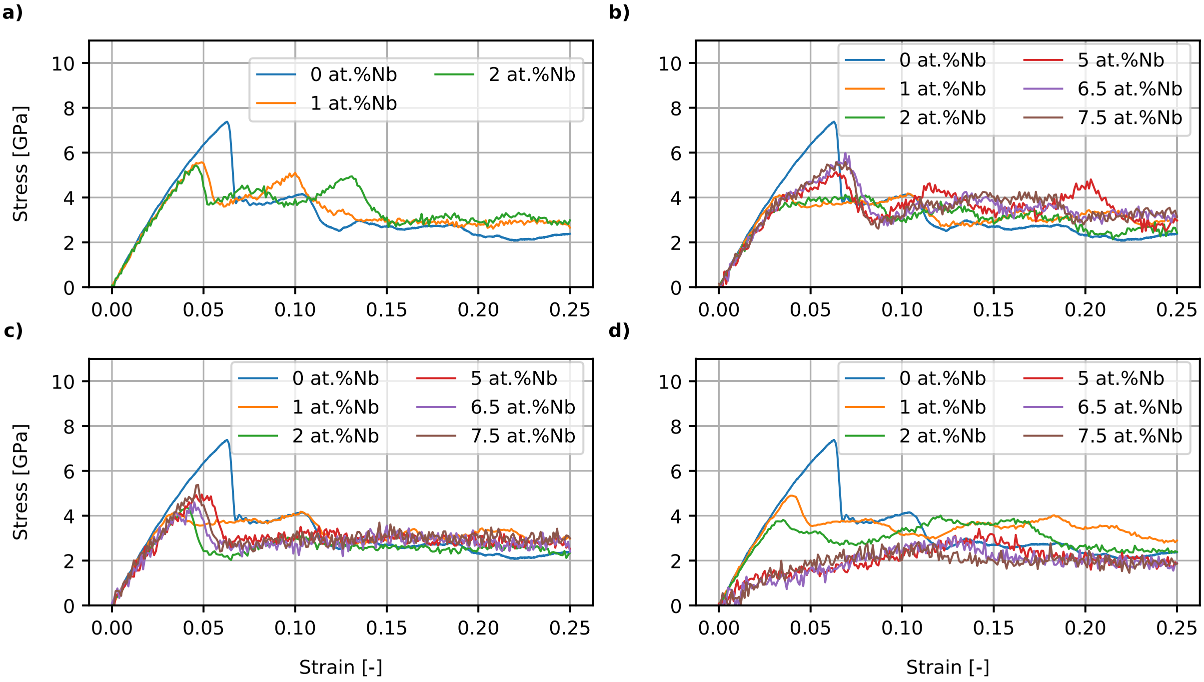

Fig. 11. The stress-strain curves for the γ/α_2 interface with Nb distributed a) near the Interface, b) in Phase B (α_2), c) in Phase A (γ), and d) homogeneously. Herein, the tension tests were performed at 700 K at a strain rate of 10^9 /s.

Table 3

Ultimate Tensile Strength [GPa] computed for the interface models with varying Nb concentrations from tension tests at 700 K and 900 K. For each interface model, we chose four sub-models with different spatial Nb distribution. Notations A, B, Interface, and Homogeneous denote Nb alloying in Phase A (γ-TiAl), Phase B (α_2-Ti$_3$Al, γ_{PT}, γ_{TT}, γ_{RB}), at the interface and homogeneously distributed, respectively.

Model	Nb conc (at.%)	UTS at 700 K				UTS at 900 K			
		A	B	Interface	Homogeneous	A	B	Interface	Homogeneous
	0	7.36				6.30			
γ/α_2	1	5.54	4.17	5.57	4.89	4.92	3.80	4.94	4.25
	2	4.37	4.20	5.43	4.01	4.68	4.08	4.56	3.40
	5	4.95	5.13		3.41	4.65	4.60		2.63
	6.5	4.60	5.99		3.07	4.75	4.98		2.30
	7.5	5.38	5.58		2.83	4.88	4.36		2.06
	0	8.57				7.45			
γ/γ_{PT}	1	6.01	4.76	6.08	5.24	5.33	4.62	5.28	4.62
	2	5.52	5.72	5.95	4.88	4.90	4.87	5.17	4.13
	5	5.47	5.62		3.12	4.95	5.15		2.69
	6.5	4.82	5.65		2.73	4.77	5.28		2.41
	7.5	5.60	5.89		2.67	4.88	5.04		2.36
	0	8.78				8.16			
γ/γ_{TT}	1	5.71	5.98	6.84	5.36	5.28	5.46	6.72	4.60
	2	5.16	5.71	7.39	5.83	5.21	5.35	6.53	4.89
	5	5.79	6.08		3.93	5.65	5.93		3.05
	6.5	6.32	5.95		3.25	5.26	5.71		2.57
	7.5	6.48	6.19		3.10	5.40	6.38		2.27
	0	6.69				5.78			
γ/γ_{RB}	1	5.05	5.23	5.81	5.03	4.71	5.01	4.80	4.76
	2	4.43	4.99	5.38	4.78	3.92	4.51	5.00	4.26
	5	4.45	4.68		3.00	3.96	3.98		2.92
	6.5	4.64	4.82		2.92	4.43	4.59		2.42
	7.5	4.93	5.04		2.70	4.79	5.04		2.20

3.2.1. Effect of Nb in single-lamellar interface models

We alloyed four different single-lamellar interface models (one γ/α_2 and three γ/γ as shown e-h in Fig. 1) with varying Nb concentrations, i.e., 1.0, 2.0, 5.0, 6.5 and 7.5 (at.%). The atomistic models were initially equilibrated to target temperatures of 300 K, 500 K, 700 K, and 900 K. Then, we applied uniaxial loading conditions along the Z direction at a strain rate of 10^9/s. The resulting stress-strain curves for the γ/α_2 interface model are given in Fig. 11. Similar to our previous single-phase models, we observed fluctuations in stress-strain curves resulting from Nb alloying.

Table 3 shows the UTS values computed for the four interface models (Fig. 1) along with their subcategories a) Nb-rich phase/bulk, b)

Table 4

Computed total dislocation density (10^{17} m^{-2}) of single-lamellar interface model of γ/α_2 with increasing Nb concentration computed at 20 ps of the tensile simulations.

Nb conc (at.%)	A	B	Interface	Homogeneous
1 at.%	1.18	1.18	2.24	1.17
2 at.%	1.48	1.15	2.23	0.68
5 at.%	1.49	1.14		0.26
6.5 at.%	2.27	1.64		0.11
7.5 at.%	1.64	1.53		0.05

Nb-rich interface, c) Nb homogeneously distributed as discussed in subsection 2. For comparison, we included the strength of Nb-free models to evaluate the predictive ability of Farkas' potential. Among the Nb-free models, $\gamma/\gamma_{\mathrm{TT}}$ showed superior strength followed by $\gamma/\gamma_{\mathrm{PT}}$,$\gamma/\alpha_2$ and $\gamma/\gamma_{\mathrm{RB}}$. In our previous work [39], the computed yield stress for single lamellar interface models showed the following trend $\gamma/\alpha_2 > \gamma/\gamma_{\mathrm{PT}} > \gamma/\gamma_{\mathrm{TT}} > \gamma/\gamma_{\mathrm{RB}}$.

It is worth noting that our two works encompassing single-lamellar interface models contain considerable differences spanning atomistic model dimensions, lattice constants of the constituent intermetallic phases, i.e., γ, α_2 (different potentials), and of course, boundary conditions (uniform deformation of simulation box (this work) vs. boundary driven deformation (previous work). Despite these differences in the simulation conditions, the observed relation showed a swap only between two interface models, i.e., γ/α_2 and γ/γ_{TT}. This swap in observed relation among the single interface model strength between our two works using Zope (previous [39]) and Farkas (this work) stems from the fact that Farkas potential showed a low UTS value for α_2 intermetallic phase. Herein, the UTS values obtained for α_2-Ti_3Al differ between two interatomic potentials, whereas for γ-TiAl, the UTS values obtained were similar (Fig. 4). This difference in the UTS values from constituent lamellae contributes to the change in the hierarchy of the strength values of γ/α_2.

Note that Farkas' potential combines two binary potentials (i.e., Nb-Ti and Ti-Al) and was mainly developed for the orthorhombic phase (Ti_2AlNb) so that some of the Nb-free models studied here may be challenging for Farkas' potential so that for such models Zope's potential may be more trustworthy.

Furthermore, Table 3 shows that each interface model followed the same hierarchy: Nb-rich interface (herein, for 1.0 at.% and 2.0 at.%) > Nb-rich phase/bulk > Nb homogeneously distributed. We observed that except for some of the homogeneously distributed Nb configurations and Nb-rich interfaces, the UTS values generally increased with Nb concentration (except when compared to 0.0 at.% Nb). Considering such irregularities, one has to keep in mind the limitations of our models. Our simulations of atomistic single interface models assume some degree of idealization by eliminating the contributions of grain boundaries, secondary alloying elements, processing-induced defects, and diffusion-dominated mechanisms. Also recall that we considered Nb substitution only at Ti sites based on site-preference energy obtained using DFT calculations. Here, we investigated atomistic models with Nb concentrations up to 7.5 at.% for both Nb-rich phase/bulk and homogeneously distributed Nb categories. However, only Nb concentrations until 2.0 at.% were feasible for Nb-rich interface models. Note that such transferability limit of the Farkas potential (until 2.0 at.% Nb) could have some implication on the physical fidelity; however, it is valid only for the special cases of atomistic models that contain high local Nb distribution in the vicinity of sharp boundaries, e.g., lamellar interfaces and colony boundaries. Due to this implication, simulating Nb-rich interface models above 2.0 at.% Nb were not feasible using Farkas potential, as shown in Table 3.

Fig. 12 sheds light on the nanomechanical events during the simulated uniaxial tension tests. We computed the atomic shear strain in the γ and α_2 phases of the single interface model without Nb (Fig. 12 a-d) and with Nb (Fig. 12 e-p). Some dislocations originated in the α_2 phase, then slowly propagated to the interface and then to γ phase (yellow arrows). One possible explanation could be that the dislocation originating in the α_2 phase was due to the fact that Farkas' potential yields relatively low UTS values for the α_2-Ti_3Al phase (Fig. 4). In Fig. 12 n-p, we could observe that the dislocations which originated in α_2 phase, while propagating to the γ phase, suffer obstructions at the interface and the remaining dislocations get dissipated/annihilated in the Nb-alloyed region of the α_2 phase. This indicates a strengthening effect, where the Nb atoms hinder the propagating dislocations. We could also observe regions of high strain (red regions in Fig. 12 l and p), resulting from dislocation gliding. From nanomechanical simulations as illustrated in Fig. 12, we extracted the total dislocation density of four types of a single interface γ/α_2. As shown in Table 4, the dislocation density reflected (with just one exception) exactly the same increases and decreases observed for the UTS in Table 3. This underlines, that the differences in the UTS can be attributed to differences in dislocation density, and the previous discussion of Fig. 12 suggests that the reason for the different dislocation densities is a hindering effect of Nb atoms, for example, for dislocation propagation.

Table 5

Dislocation density of MIAMs for different Nb concentrations at 700 K.

Timsteps (ps)	Total dislocation density ($\times 10^{16}$m^{-2})		
	0 at.% Nb	0.5 at.% Nb	1 at.% Nb
0	4.5085	4.5974	5.8045
15	4.5657	4.6878	5.8630
30	4.6064	5.3535	8.2365
45	5.3364	7.2416	9.9968
60	7.2820	7.9126	10.5955
75	8.5360	8.6321	11.5630
90	9.4767	9.5895	12.1548

In this subsection, we investigated the influence of Nb alloying on the single-interface models and their variants. We found that a concentration of Nb atoms around the interface was particularly beneficial for the UTS compared to a wider distribution of the Nb atoms in one or both phases. The order of the UTS of the Nb-enriched interfaces was as follows: $\gamma/\gamma_{\mathrm{TT}} > \gamma/\gamma_{\mathrm{PT}} > \gamma/\alpha_2 > \gamma/\gamma_{\mathrm{RB}}$. A nanomechanical analysis suggested that the hindering of dislocation propagation by Nb atoms around the interface may play a key role in the beneficial effect that Nb atoms around the interface have on the UTS. Generally, Nb alloying reduced the UTS compared to Nb-free models in the Nb concentration regime studied.

3.2.2. *Effect of Nb alloying in MIAMs*

We further investigated the effects of Nb alloying on microstructure-informed atomistic models (MIAMs). Here, we considered two global Nb concentrations (0.5 at.% and 1.0 at.%) by substituting Nb at random Ti sites. After equilibrating the simulation models to their target temperatures (300 K, 500 K, 700 K and 900 K), we simulated uniaxial loading along the Z direction at a strain rate of 10^9/s.

Fig. 13 shows the stress-strain curves of MIAMs at selected temperatures and Nb concentrations. Similar to single intermetallic phases (section 3.1.2) and interface models (section 3.2.1), the UTS of MIAMs decreased with Nb alloying. Furthermore, Nb-free MIAMs at all temperatures showed UTS, followed by a considerable drop in stress at relatively low strains. In contrast, for MIAMs containing 1.0 at.% Nb, UTS was achieved with much higher strains and not followed by a similarly clear drop of stress, indicating improved ductility at the nanoscale. In other words, Nb alloying delayed the failure point in MIAMs, particularly at high temperatures and high Nb concentrations (1 at.%).

To unravel the nanomechanical origin of improved ductility (enhanced dislocation activities) with Nb alloying, we computed the dislocation density of MIAMs both qualitatively (Fig. 14) and quantitatively (Table 5) during the simulated tension tests. Table 5 shows the increasing dislocation densities with Nb computed at selected time steps during

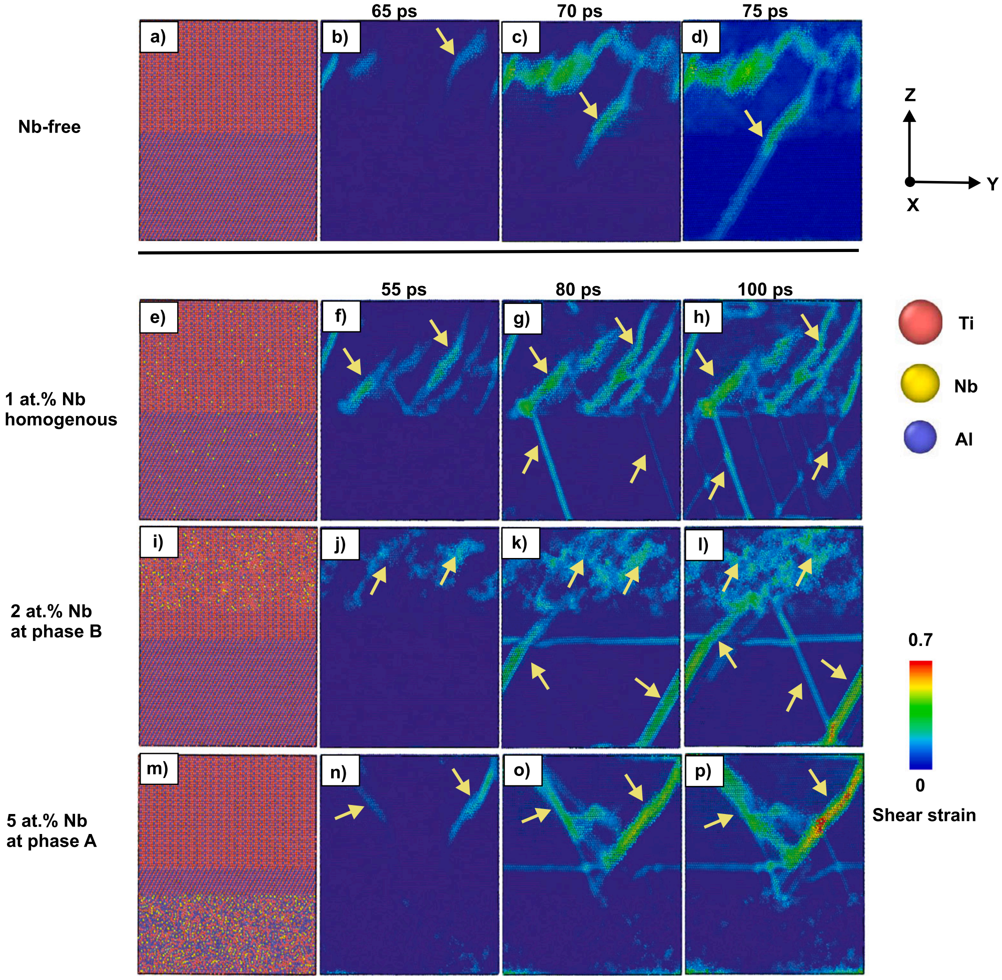

Fig. 12. Atomic shear strain distribution of γ/α_2 interface models from tension tests (strain rate: 10^9 /s, T = 700 K) at selected time steps for a Nb-free model (a-d), 1.0 at.% Nb homogeneously distributed (e-h), 2.0 at.% Nb distributed in phase A, i.e., α_2-Ti$_3$Al (i-l), and 5.0 at.% Nb distributed in phase A, i.e., γ-TiAl (m-p). The yellow markers denote the dislocations.

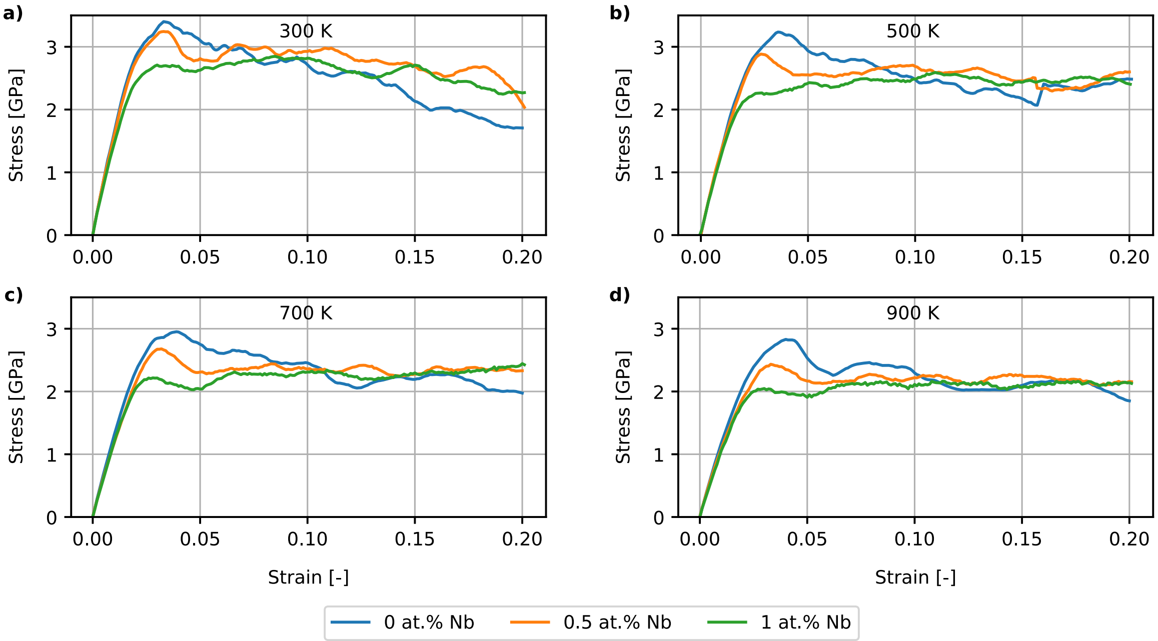

Fig. 13. The stress-strain curves for MIAMs with 0.0% Nb, 0.5% and 1.0% Nb from tension tests with a strain rate of 10^9 /s at selected temperatures (300 K, 500 K, 700 K, and 900 K.)

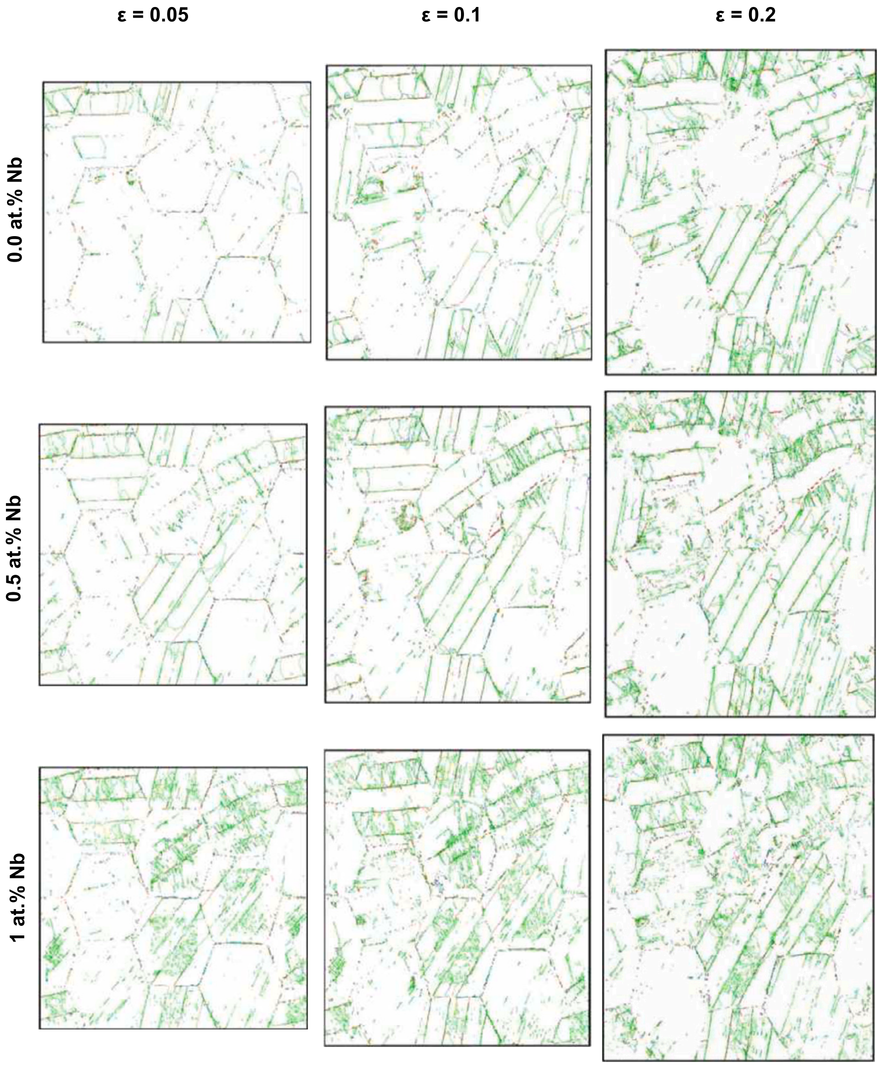

Fig. 14. Dislocation evolution in MIAMs with varying Nb concentrations of 0.0 at.% Nb (top), 0.5 at.% Nb (middle) and 1.0 at.% Nb (bottom) under thermo-mechanical loading at 900 K observed at strain values of 0.05 (left), 0.1 (center) and 0.2 (right).

increasing tension at 700 K. Note that the relative increase in dislocation density remains high with Nb alloying, explaining improved ductility with Nb addition. Fig. 14 shows that the Nb-free model exhibits at large strains mostly interface-dominated dislocations, whereas for increasing Nb content, more intra-lamellar dislocations are observed. Our MIAMs (1.0 at.%) showed that Nb facilitated the early onset of dislocations even at a much lower strain of $\epsilon = 0.05$ at 900 K. Nb alloying delayed the failure point in MIAMs, particularly at high temperatures and high Nb concentrations (1 at.%). Fig. 15 shows the interplay between Nb alloying and temperature in reducing the occurrence of intergranular fracture (the reason behind the stress drop after UTS) along the colony boundaries. Apparently, the fracture is delayed, and dislocation activities are increased both by Nb alloying and increasing temperature.

Table 6
HCP structure volume fraction of MIAMs during tension tests (strain rate = 10^9 /s, T = 700 K.) for different points in time with Nb concentrations.

MIAM colony type	Nb concentration [at. %]	Simulated time [ps]		
		30	60	90
$\gamma/\gamma_{\mathrm{RB}}$	0	10.5	14.6	15.2
	0.5	10.5	14.4	15.0
	1	8.5	12.4	14.8
γ/α_2	0	43.6	41.5	39.4
	0.5	40.1	39.9	38.8
	1	38.5	39.3	36.3
$\gamma/\gamma_{\mathrm{TT}}$	0	7.6	7.4	8.7
	0.5	9.1	10.9	13.6
	1	7.4	11.7	15.9
$\gamma/\gamma_{\mathrm{PT}}$	0	10.1	14.2	14.4
	0.5	10.2	15.1	16.1
	1	11.2	17.2	19.7

Stress-induced transformation of γ (face-centered tetragonal [FCT] atoms) to α_2 (hexagonal close packed [HCP] atoms) in TiAl-based alloys was studied in several works [80–83]. Note that the stress-induced α_2 phase has different lattice parameters compared to the ordered hexagonal α_2 (DO_{19}) phase. As we simulated tension with Nb-free MIAMs, stress-induced $\gamma \rightarrow \alpha_2$ transformation occurred in most γ phases and their variants γ_{PT}, γ_{TT}, γ_{RB}. We computed the volume fraction of HCP atoms to analyze this transformation (Table 6). As shown in Table 6, the HCP volume fraction decreased for $\gamma/\gamma_{\mathrm{RB}}$ and γ/α_2 with an increase in Nb concentration, whereas a reverse trend was observed for both $\gamma/\gamma_{\mathrm{TT}}$ and $\gamma/\gamma_{\mathrm{PT}}$ colonies. [80] observed a similar discrepancy in the trend reporting that the stress-induced $\gamma \rightarrow \alpha_2$ transformation primarily occurred at twin intersections and in twinned regions.

To examine whether this phenomenon occurs also in our simulations, we focus specifically on the colonies representing each case γ/γ_{TT}

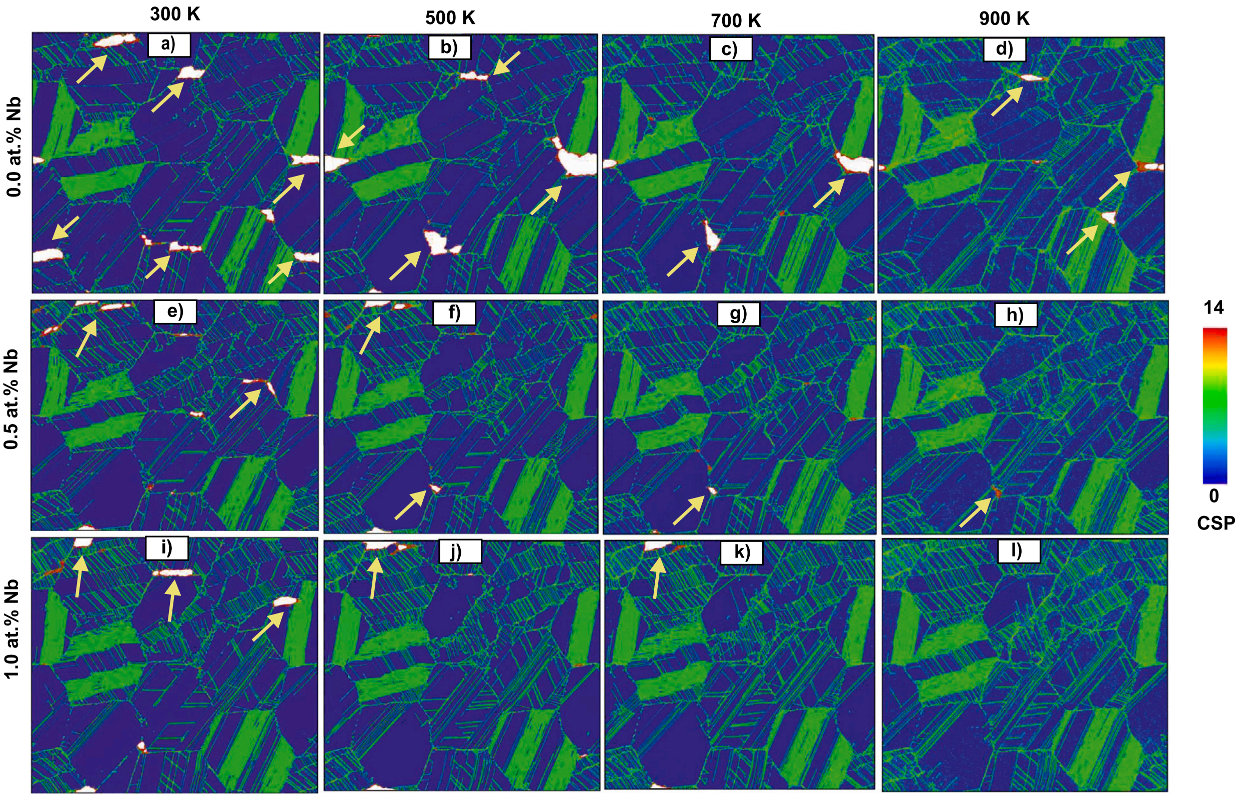

Fig. 15. MIAMs with Nb concentrations of 0.0 at.% Nb (top), 0.5 at.% Nb (middle) and 1.0 at.% Nb (bottom) deformed at temperatures of (from left to right) 300 K, 500 K, 700 K, and 900 K after 200 ps. The yellow markers indicate the intergranular fracture along the colony boundaries.

and γ/γ_{RB} lamellae. In Fig. 16, the microstructure evolution of the γ lamella and the adjacent γ_{TT} lamellae with varying Nb concentrations are shown. During simulated tension, MIAMs with Nb exhibited several dislocation gliding events and twinning (black arrows in Fig. 16), thus contributing to the enhanced HCP volume fraction in these colonies. Nb alloying facilitates the stacking fault formation, and the dislocations glided parallel and oblique to the lamellar interfaces as shown in Fig. 16 d, k, and l. MIAMs with Nb exhibited significantly more dislocations and twins at the same strain. An enlarged view of one of the twin boundaries (γ region of γ_{TT} grain) is shown in Fig. 16 k. The black arrows in the figure correspond to the twin boundary region, while all other HCP regions correspond to the stacking faults traced by dislocation gliding.

Fig. 17 shows the $\gamma/\gamma_{\mathrm{RB}}$ colony at various Nb concentrations. To obtain nanomechanical insights, we focused here on a single colony of a MIAM and it is observed that the γ_{RB} region of this colony has undergone a phase transformation to α_2 (several layers of HCP atoms). The same regions in the colony during the simulations were compared to study the slow phase transformation in a sequence like 1a, 1b, and 1c, etc. Herein, Nb alloying hampered $\gamma \rightarrow \alpha_2$ transformation, thus retaining more activation regions of γ for dislocation activities to enhance the plasticity at the nanoscale, as observed in Fig. 14. Note in this respect, in particular Fig. 17 3c - 6c underlining a delayed α_2 formation by Nb.

Studying the γ/γ_{RB} lamellae (Fig. 17), we noticed stacking-faults dominated deformation with some blade-shaped bundles perpendicular to lamellar interfaces. TEM investigations of the deformed samples [84] reported similar blade-shaped bundles and stacking faults along the lamellar boundaries governing the plastic deformation. For both these mechanisms, gliding of $1/6[1\ 1\ \bar{2}]$ partial dislocations on $\{1\ 1\ 1\}$ planes act as a precursor, as observed in our MD simulations. Fig. 16 shows increasing stacking fault bundles from lamellar interfaces with Nb to relieve stress concentration. Our MD simulations (Figs. 16 and 17) showed the glide of $1/6<1\ 1\ 2>$ Shockley partial dislocations on the alternate $(1\ 1\ 1)$ plane induced the phase transformation of $\gamma \rightarrow \alpha_2$, resulting in more α_2 laths. Wen et al. [85] reported similar stress-induced γ to α_2 phase transformation of TiAl-based alloys at room temperature.

The interplay between the thermal driving force (temperature effects) and Nb solutes plays a crucial role in the deformation behavior. For instance, the Nb concentrations at room temperature did not improve the ductility, as we observed intergranular fracture near colony boundaries (Fig. 15 a, e, and i), whereas the combination of high temperature and Nb concentration stimulated the dislocation slipping and twining. These observations align with the previous arguments that several deformation mechanisms coexist in TiAl depending on the lamellae variants and their corresponding interfaces, colony orientation, Nb alloying, and temperature. In some regions (γ_{RB}, γ/α_2), Nb solutes retained the γ region to offer more dislocation sources – by retarding $\gamma \rightarrow \alpha_2$ transformation – supported by higher temperatures. In other twinned regions (γ_{PT}, γ_{TT}), Nb alloying promoted the early onset of dislocation activities at much lower strain, enhancing the ductility at the nanoscale and supported again by temperature.

Generally, in atomistic thermo-mechanical simulations of MIAMs we observed a poor room temperature ductility. In particular, Nb-free MIAMs exhibited intergranular fracture along the colony boundaries (Fig. 15). Nb alloying delayed the crack's nucleation and propagation by relieving the stress concentrations through dislocation nucleation, propagating further into adjacent colonies, thus improving the deformability. Nb alloying triggered the early onset of nanomechanical events like dislocation gliding and twinning even at moderate temperature by lattice distortions and reduced stacking fault energy, especially in the γ region and twinned lamellae variants. CNA analysis revealed that Nb alloying and temperature distorted lamellae inside the colonies, enhancing the deformability at high strains (Fig. 17). However, with increasing Nb, colonies with α_2 showed significant deformation, such as stepping behavior and colony restructuring resulting in serrated colony boundaries. Despite considering only low Nb concentrations in MIAMs, Nb enhanced the ductility of TiAl alloys, specifically at high temperatures. Herein, MD simulations of MIAMs revealed that several deformation

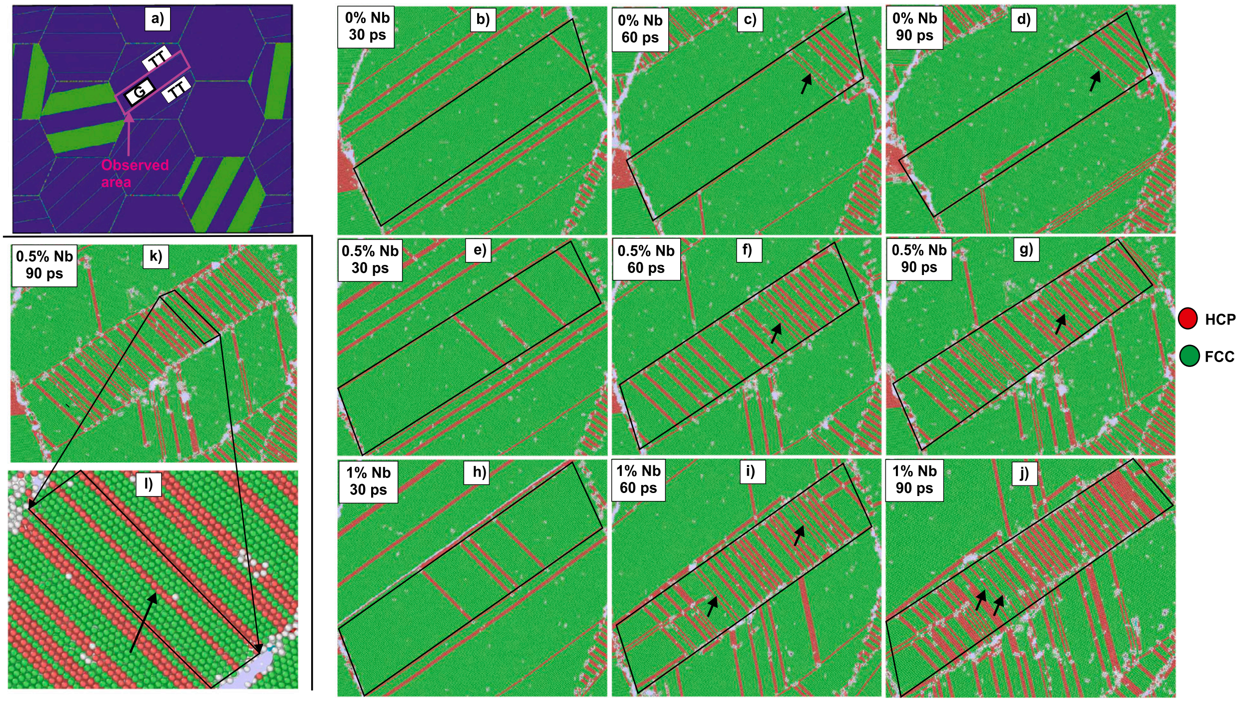

Fig. 16. The formation of mechanical twins in a γ/γ_{TT} colony of a MIAM (a) with 0.0% Nb, 0.5% Nb, and 1% Nb at (from left to right) 30 ps, 60 ps and 90 ps during tension tests at a rate of 10^9 /s. The situation for 0.5% Nb at 90 ps is depicted in detail in (k) and (l).

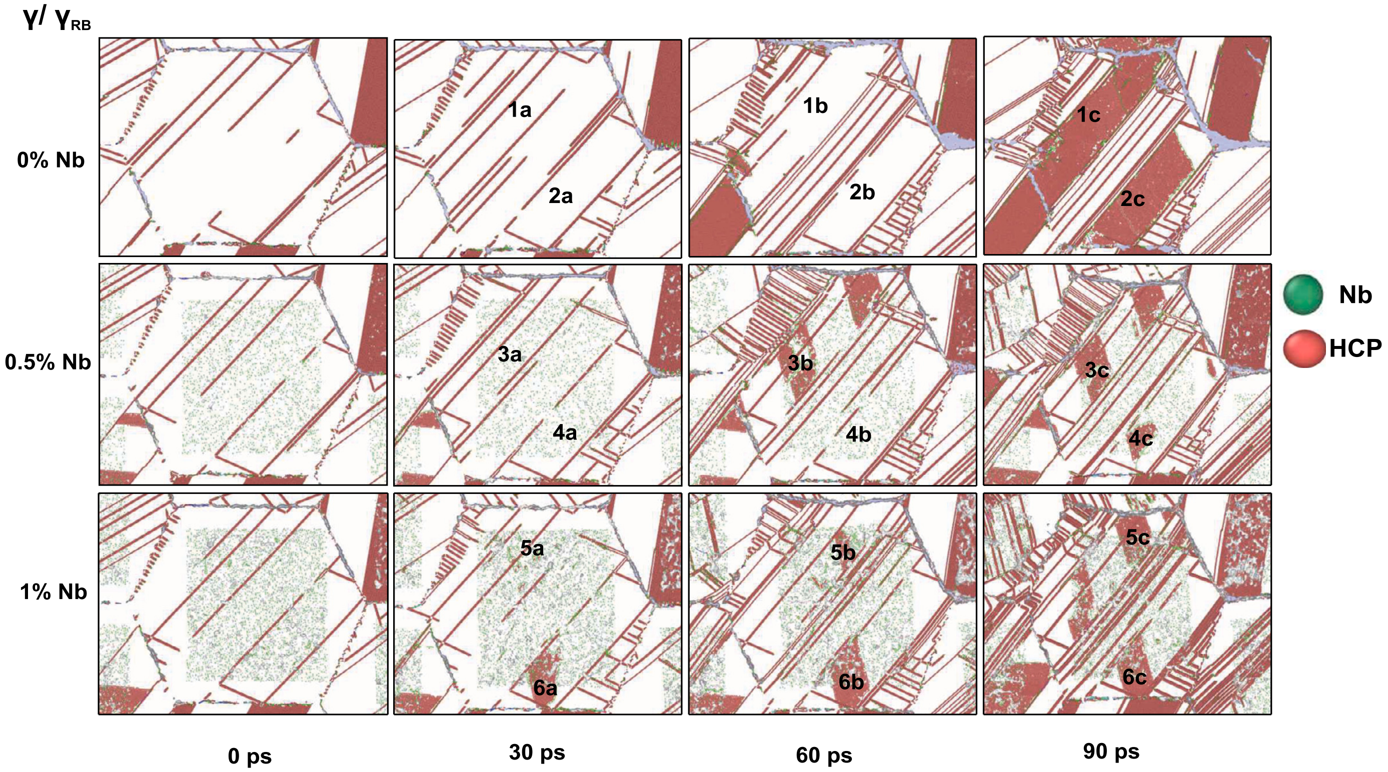

Fig. 17. Retardation of stress-induced $\gamma \rightarrow \alpha_2$ transformation observed in γ/γ_{RB} colony of MIAM with Nb concentrations of 0.0 at.% Nb (top), 0.5 at.% Nb (middle) and 1.0 at.% Nb (bottom) at (from left to right) 0 ps, 30 ps, 60 ps and 90 ps during tension test at a strain rate of 10^9 /s and at a temperature of 700 K.

mechanisms coexist depending on the volume fraction of lamellae variants and their corresponding interfaces, colony orientation, Nb alloying, and temperature. For instance, Nb hampered the stress-induced $\gamma \rightarrow \alpha_2$ transformation in γ_{RB} and γ/α_2 region to offer more dislocation sources, whereas, in other twinned regions (γ_{PT}, γ_{TT}), Nb facilitated dislocation activities at low strains resulting in some finer lamellae increasing the interface volume fraction. Note that our study supports that Nb addition promotes dislocation gliding and twinning in TiAl-based alloys as it lowers the stacking fault energy of γ-TiAl [1]. Experimental estimates suggest a typical Nb concentration of 5 - 10 at.% to achieve improved mechanical properties, exhibiting superior strength and ductility.

MIAMs with Nb showed microstructure refinement (fine lamellae creation) due to reduced stacking fault energy as a precursor for dislocation formation. Generally, the UTS values decreased with Nb concentration for all the atomistic models (i.e., single phase models, single lamellar interface models, MIAMs) studied herein with some exceptions, as discussed in 2.1.3. Furthermore, the computed dislocation densities were consistent with the observed trend in UTS, indicating a strong correlation between them. In single-lamellar interface models, the hindrance of dislocation motion by Nb atoms around the interface explains their effects on the UTS. To this end, the proximity of Nb atoms to microstructure boundaries (e.g., interfaces) appeared to play an important role, and similarly the ratios of twin boundaries and phase boundaries. Increasing dislocation activities with increasing Nb concentration suggest that improved mechanical properties stem from the microstructural changes rather than solid-solution strengthening [86]. Note that our MD simulations revealed that Nb alloying contributed to significant lattice distortions, further influencing the dislocation evolution under thermomechanical deformation. However, we strongly emphasize the need for future studies with mixed site models, high Nb concentrations, secondary disordered phases and other similar complex interfaces, and other interatomic potential to ensure the generality of the conclusions drawn. The atomistic models studied showed a decreasing UTS with Nb alloying, which may be attributed to the lattice distortions. However, the strain corresponding to the UTS increased with Nb alloying, particularly at high temperatures (900 K) for the MIAMs (1.0 at.% Nb) studied herein. Thus, combining our insights, Nb alloying improved ductility to some extent at the cost of strength [86].

4. Conclusions

This work investigated the effect of Nb alloying on the strength and ductility of TiAl-based alloys under thermo-mechanical conditions using atomistic simulations. Using single-phase models, we first confirmed the transferability of Farkas' ternary potential in our study by computing quantities such as elastic constants, point defect formation energies, and cohesive energies and by comparing them to two other binary interatomic potentials for TiAl-based alloys. It turned out that Farkas' ternary potential can capture also the behavior of binary intermetallic phases (i.e., γ-TiAl and α_2-Ti$_3$Al). This ensured us that we could use it also in studies where in the same type of model, the Nb concentration was increased from zero (binary system) to a substantial fraction (ternary system).

Our DFT calculations reaffirmed a known site preference of Nb at Ti sites over Al sites. Analyzing the PDOS suggested a weakening of Ti(3d)-Al(3p) interactions by Nb addition resulting in increased ductility in γ-TiAl and α_2-Ti$_3$Al.

Both in interface models and more complex microstructure-informed atomistic models (MIAMs), we observed that the ultimate tensile strength (UTS) was decreased by Nb. However, the maximal strain associated with UTS was increased by Nb due to the associated higher ductility. Our molecular dynamics (MD) simulations identified several nanomechanical mechanisms behind this effect, such as the delay of fracture onset by increased dislocation formation and propagation that relieved some stress without fracture. Also, Nb was found to hamper the stress-induced $\gamma \rightarrow \alpha_2$ transformation in γ_{RB} and γ/α_2, hence favoring a situation with more dislocation sources. In other twinned regions (γ_{PT}, γ_{TT}), Nb facilitated dislocation activities at low strain, resulting in finer lamellae increasing the interface volume fraction.

Our atomistic simulations underlined the important role of microstructure boundaries (i.e., lamellar interfaces and colony boundaries) because many of the mechanisms how Nb altered mechanical properties appeared closely related to microstructural boundaries. They thus present an important means of optimizing the thermo-mechanical properties of TiAl-based alloys. At low Nb concentrations, we obtained the novel insight that Nb assists in delaying the $\gamma \rightarrow \alpha_2$ phase transformation to improve ductility, besides the widely reported solid-solution strengthening (dislocations pinned/retarded by Nb) and microstructure changes.

For the low Nb concentrations we studied, we found that Nb helped to improve ductility, though to some extent at the cost of strength. The experimental investigations suggest that a high Nb concentration of 5 - 10 at.% leads to both high strength and ductility. Examining whether or how the thermo-mechanical properties change at higher Nb concentrations would be an important next step but may first require the development of enhanced interatomic potentials that can handle higher Nb fractions for atomistic models with complex microstructure.

CRediT authorship contribution statement

Anju Chandran: Conceptualization, Data curation, Investigation, Methodology, Software, Visualization, Writing – original draft. **Hariprasath Ganesan:** Conceptualization, Funding acquisition, Investigation, Methodology, Project administration, Supervision, Visualization, Writing – review & editing. **Christian J. Cyron:** Funding acquisition, Supervision, Validation, Writing – review & editing.

Declaration of competing interest

The authors declare that they have no known competing financial interests or personal relationships that could have appeared to influence the work reported in this paper.

Data availability

Data will be made available on request.

Acknowledgements

AC, HG, and CC gratefully acknowledge the funding through the I^{2}B project MetalMD at Helmholtz-Zentrum Hereon, Germany. AC and HG thank Prof. Wanlin Guo and Henggao Xiang for sharing the newly developed interatomic potential of Nb-Ti-Al systems to realize some comparison simulations in this study. AC and HG acknowledge the fruitful discussions with Dirk Steglich and Ingo Scheider on ductility at the nanoscale.

Appendix A

Additional information on [32]: the Kim potential is a second nearest neighbor Modified Embedded Atomic Model (MEAM). This potential reproduced the lattice parameters with errors within 0.5%. The Kim and Zope potential produced comparable cohesive energy values. The elastic constants C_{11} and C_{12} calculated using the Kim potential showed good agreement with the experimental values.

Additional information on [33]: Xiang and Guo [33] proposed a ternary potential of NbAlTi systems based on a MEAM. The authors have studied TiAlNb systems with Nb concentrations up to 10.0 at.%. Here the site of substitution of Nb was a mixture of both Ti and Al lattice sites. They studied the melting point and high-temperature deformation properties of γ and α_2 systems containing Nb and computed the elastic moduli and generalized stacking faults (GSFs) of Nb-alloyed γ and α_2. The high-temperature deformed structure contained stacking faults (SFs) and twins, and they compared the stress-strain curve for various Nb concentrations.

Our observation on the lattice constant (Fig. 18) 'a' differs from [61], where they observed an increase in 'a' with Nb (8 at.%) for α_2-Ti$_3$Al. We believe that the discrepancy may stem from the difference in Nb concentration and Nb substitution sites assumed for alloying (i.e., our work considered only Ti sites and [61] might have considered both Ti and Al sites but not explicitly stated).

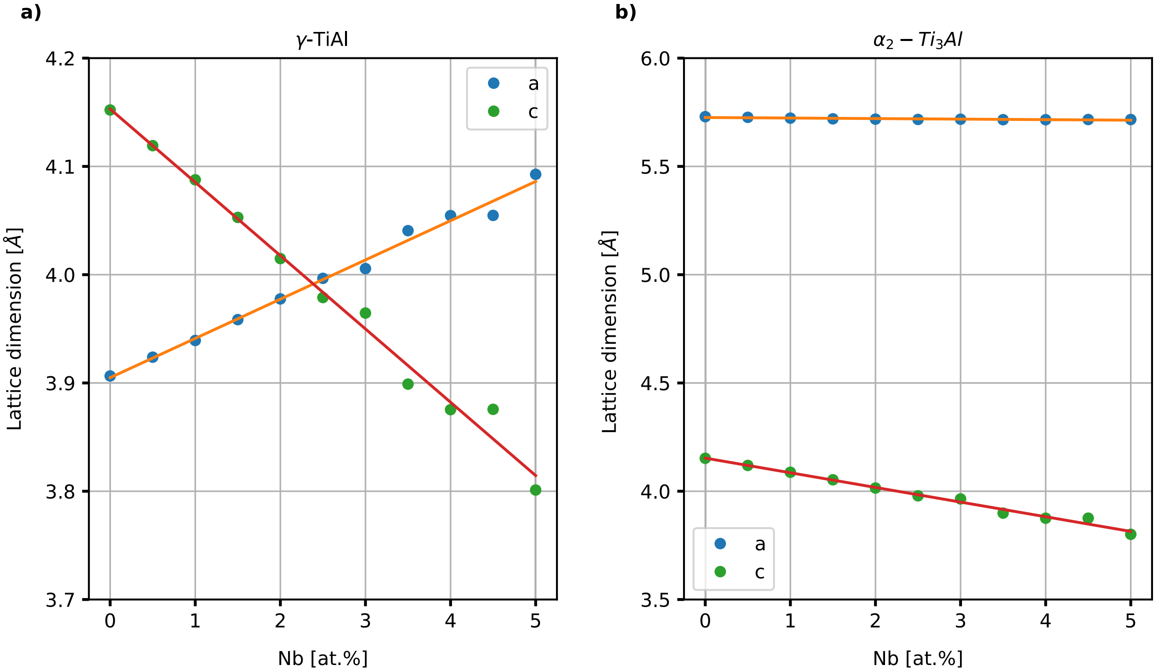

Fig. 18. The change in lattice parameters 'a' and 'c' with increasing Nb concentration in a) γ-TiAl and b) α_2-Ti$_3$Al computed using Farkas' ternary potential [57].

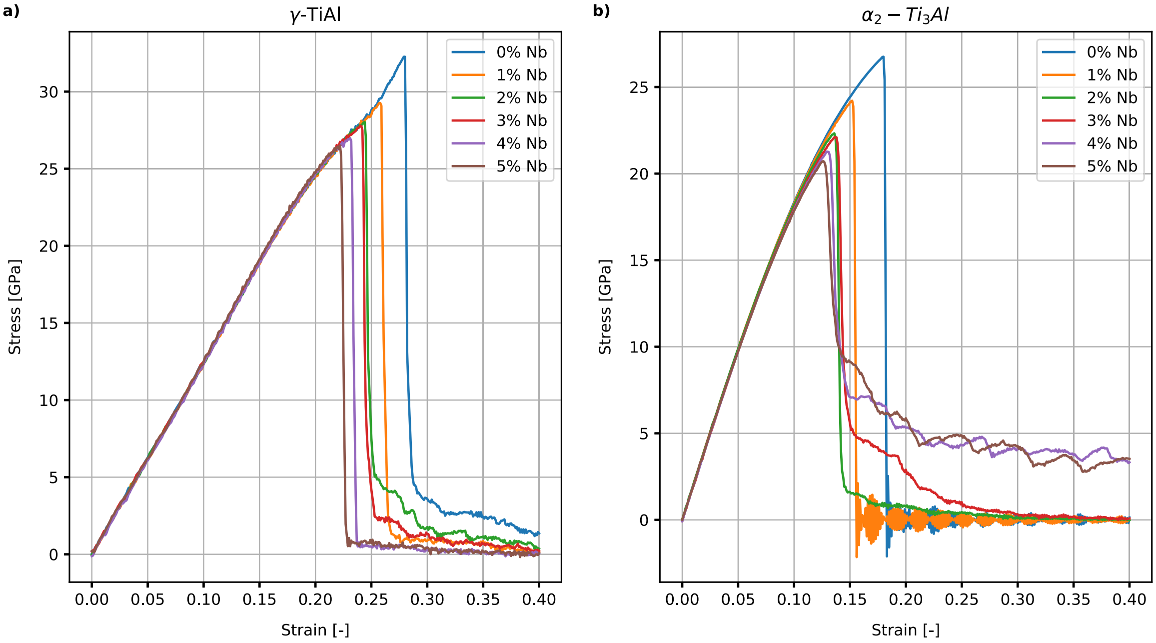

Fig. 19. Stress-strain curves for single phase systems with varying Nb concentrations using Xiang's interatomic potential [33].

We simulated tension tests to evaluate the mechanical behavior of single phase models of γ-TiAl and α_2-Ti$_3$Al using Xiang potential [33](refer Fig. 19) We applied a strain rate of 10^9/s and the models were equilibrated at 300 K. The stress-strain curves present a contradiction to our previous observation (Fig. 10) using Farkas potential [31]. In our current study, we noted a decrease in UTS with increasing Nb concentration. Xiang potential [33] showed a decreasing trend in both UTS and ductility upon Nb introduction. However, this observation requires further investigation using Xiang potential, which is beyond the scope of this article.

We simulated tension tests on the interface models with varying Nb concentrations (1.0, 2.0, 5.0, 6.5, and 7.5 (at.%)) using Xiang potential (Table 7). We applied a strain rate of 10^9/s, and the models were equilibrated at 700 K. The UTS showed a comparable trend to that observed in interface models using Farkas potential (refer 3.2.1).

References

[1] Fritz Appel, Jonathan David Heaton Paul, Michael Oehring, Gamma Titanium Aluminide Alloys: Science and Technology, John Wiley & Sons, 2011.

[2] Helmut Clemens, Svea Mayer, Design, processing, microstructure, properties, and applications of advanced intermetallic TiAl alloys, Adv. Eng. Mater. 15 (4) (2012) 191–215.

[3] Jianbo Li, Yong Liu, Bin Liu, Yan Wang, Kun Zhao, Yuehui He, Effect of nb particles on the flow behavior of TiAl alloy, Intermetallics 46 (2014) 22–28.

[4] O. Ostrovskaya, C. Badini, S.M. Deambrosis, E. Miorin, S. Biamino, E. Padovano, Protection from oxidation of second and third generation TiAl intermetallic alloys

Table 7
Ultimate Tensile Strength [GPa] computed for the interface models with varying Nb concentrations from tension tests at 700 K using Xiang's potential [33]. For each interface model, we chose four sub-models with different spatial Nb distributions. Notations A, B, Interface, and Homogeneous denote Phase A (γ-TiAl), Phase B (α_2-Ti_3Al, γ_{PT}, γ_{TT}, γ_{RB}), interface and homogeneous, respectively.

Model	Nb conc (at.%)	700 K			
		A	B	Int	Total
	0	18.20			
γ/α_2	1	18.17	15.19	11.43	16.53
	2	16.06	12.51	10.05	15.13
	5	13.09	10.86		14.67
	6.5	11.61	9.49		14.33
	7.5	11.19	8.68		13.91
	0	20.07			
γ/γ_{PT}	1	19.35	15.10	15.74	21.33
	2	17.08	12.85	12.38	15.69
	5	12.37	9.72		18.19
	6.5	12.61	7.92		16.17
	7.5	10.64	9.26		14.68
	0	21.56			
γ/γ_{TT}	1	18.77	17.47	14.61	18.44
	2	16.67	14.48	11.20	17.93
	5	12.37	9.72		18.19
	6.5	11.32	8.96		15.27
	7.5	11.08	8.35		14.65
	0	21.66			
γ/γ_{RB}	1	20.72	14.14	17.65	15.78
	2	18.59	14.01	13.45	15.10
	5	14.21	12.06		12.35
	6.5	12.96	12.32		11.39
	7.5	12.31	11.17		11.84

by magnetron sputtering deposition of a TiAl/TiAlN coating, Mater. Des. 208 (2021) 109905.

[5] Thomas Klein, Helmut Clemens, Svea Mayer, Advancement of compositional and microstructural design of intermetallic γ-TiAl based alloys determined by atom probe tomography, Materials 9 (9) (2016) 755.

[6] S.Z. Zhang, C.J. Zhang, Z.X. Du, Z.P. Hou, P. Lin, F.T. Kong, Y.Y. Chen, Deformation behavior of high Nb containing TiAl based alloy in $\alpha + \gamma$ two phase field region, Mater. Des. 90 (2016) 225–229.

[7] F. Appel, M. Oehring, R. Wagner, Novel design concepts for gamma-base titanium aluminide alloys, Intermetallics 8 (9–11) (2000) 1283–1312.

[8] Z.C. Liu, J.P. Lin, S.J. Li, G.L. Chen, Effects of Nb and Al on the microstructures and mechanical properties of high nb containing TiAl base alloys, Intermetallics 10 (7) (2002) 653–659.

[9] F. Appel, J.D.H. Paul, M. Oehring, U. Fröbel, U. Lorenz, Creep behavior of TiAl alloys with enhanced high-temperature capability, Metall. Mater. Trans. A 34 (10) (2003) 2149–2164.

[10] Bin Zhu, Xiangyi Xue, Hongchao Kou, Xiaolei Li, Jinshan Li, Effect of microstructure on the fracture toughness of multi-phase high Nb-containing TiAl alloys, Intermetallics 100 (2018) 142–150.

[11] Lin Song, Fritz Appel, Li Wang, Michael Oehring, Xingguo Hu, Andreas Stark, Junyang He, Uwe Lorenz, Tiebang Zhang, Junpin Lin, Florian Pyczak, New insights into high-temperature deformation and phase transformation mechanisms of lamellar structures in high Nb-containing TiAl alloys, Acta Mater. 186 (2020) 575–586.

[12] G.L. Chen, L.C. Zhang, Deformation mechanism at large strains in a high-Nb-containing TiAl at room temperature, Mater. Sci. Eng. A 329–331 (2002) 163–170.

[13] Liang Cheng, Jinshan Li, Xiangyi Xue, Bin Tang, Hongchao Kou, Emmanuel Bouzy, Superplastic deformation mechanisms of high Nb containing TiAl alloy with ($\alpha 2 + \gamma$) microstructure, Intermetallics 75 (2016) 62–71.

[14] Fu-Sheng Sun, Chun-Xiao Cao, Ming-Gao Yan, Seung-Eon Kim, Yong-Tailee, Alloying mechanism of beta stabilizers in a TiAl alloy, Metall. Mater. Trans. A 32 (7) (2001) 1573–1589.

[15] M. Weller, H. Clemens, G. Haneczok, G. Dehm, A. Bartels, S. Bystrzanowski, R. Gerling, E. Arzt, Mechanical spectroscopy of a high-Nb-bearing γ-TiAl-based alloy with near-gamma and fully lamellar microstructure, Philos. Mag. Lett. 84 (6) (2004) 383–393.

[16] F. Appel, M. Oehring, J.D.H. Paul, Nano-scale design of TiAl alloys based on β-phase decomposition, Adv. Eng. Mater. 8 (5) (2006) 371–376.

[17] Xin Yang, Zheng ping Xi, Yong Liu, Hui ping Tang, Ke Hu, Wen peng Jia, Microstructure and fracture toughness of a TiAl-Nb composite consolidated by spark plasma sintering, Trans. Nonferr. Met. Soc. China 22 (11) (2012) 2628–2632.

[18] Pei Liu, Bo Hou, Aiqin Wang, Jingpei Xie, Zhenbo Wang, Balancing the strength and ductility of Ti2AlC/TiAl composite with a bioinspired micro-nano laminated architecture, Mater. Des. 220 (2022) 110851.

[19] Hong Zhang, Dong Lu, Yubing Pei, Tan Chen, Tongfei Zou, Tianjian Wang, Xiaoyan Wang, Yongjie Liu, Qingyuan Wang, Tensile behavior, microstructural evolution, and deformation mechanisms of a high Nb-TiAl alloy additively manufactured by electron beam melting, Mater. Des. 225 (2023) 111503.

[20] J.D.H. Paul, F. Appel, R. Wagner, The compression behaviour of niobium alloyed γ-titanium aluminides, Acta Mater. 46 (4) (1998) 1075–1085.

[21] G.L. Chen, X.T. Wang, K.Q. Ni, S.M. Hao, J.X. Cao, J.J. Ding, X. Zhang, Investigation on the 1000, 1150 and 1400°C isothermal section of the tialnb system, Intermetallics 4 (1) (1996) 13–22.

[22] M. Yoshihara, K. Miura, Effects of Nb addition on oxidation behavior of TiAl, Intermetallics 3 (5) (1995) 357–363.

[23] Wei Lu, ChunLin Chen, LianLong He, YanJun Xi, FuHui Wang, Effect of niobium on the oxidation behavior of TiAl, J. Mater. Res. 22 (6) (2007) 1486–1490.

[24] David Holec, Rajeev K. Reddy, Thomas Klein, Helmut Clemens, Preferential site occupancy of alloying elements in TiAl-based phases, J. Appl. Phys. 119 (20) (2016) 205104.

[25] Ye Wei, Ying Zhang, Guang-Hong Lu, Huibin Xu, Effects of transition metals in a binary-phase TiAl–Ti3Al alloy: from site occupancy, interfacial energetics to mechanical properties, Intermetallics 31 (2012) 105–113.

[26] Y. Song, R. Yang, D. Li, Z.Q. Hu, Z.X. Guo, A first principles study of the influence of alloying elements on TiAl: site preference, Intermetallics 8 (5–6) (2000) 563–568.

[27] O. Ouadah, G. Merad, F. Saidi, S. Mendi, M. Dergal, Influence of alloying transition metals on structural, elastic, electronic and optical behaviors of γ-TiAl based alloys: a comparative DFT study combined with data mining technique, Mater. Chem. Phys. 242 (2020) 122455.

[28] O. Ouadah, G. Merad, H. Si Abdelkader, Atomistic modelling of the γ-TiAl/α_2-Ti3Al interfacial properties affected by solutes, Mater. Chem. Phys. 257 (2021) 123434.

[29] Rajendra R. Zope, Y. Mishin, Interatomic potentials for atomistic simulations of the Ti-Al system, Phys. Rev. B 68 (2) (2003) 024102.

[30] D. Farkas, Interatomic potentials for Ti-Al with and without angular forces, Model. Simul. Mater. Sci. Eng. 2 (5) (1994) 975.

[31] Diana Farkas, Chris Jones, Interatomic potentials for ternary Nb - Ti - Al alloys, Model. Simul. Mater. Sci. Eng. 4 (1) (1996) 23.

[32] Young-Kwang Kim, Hong-Kyu Kim, Woo-Sang Jung, Byeong-Joo Lee, Atomistic modeling of the Ti–Al binary system, Comput. Mater. Sci. 119 (2016) 1–8.

[33] Henggao Xiang, Wanlin Guo, A newly developed interatomic potential of Nb-Al-Ti ternary systems for high-temperature applications, Acta Mech. Sin. 38 (1) (2022).

[34] S.P. Kiselev, E.V. Zhirov, Molecular-dynamics simulation of the synthesis of intermetallic Ti–Al, Intermetallics 49 (2014) 106–114.

[35] Li Wen, Yajun Yin, Qian Xu, Jianxin Zhou, Hai Nan, Xiaoyuan Ji, Xu Shen, Xin Feng, Wen Yu, Zhixin Tu, Nan Pang, Tensile behavior of $\gamma/\alpha 2$ interface system in lamellar TiAl alloy via molecular dynamics, Comput. Mater. Sci. 159 (2019) 397–402.

[36] Fu-Ling Tang, Hou-Min Cai, Hong-Wei Bao, Hong-Tao Xue, Wen-Jiang Lu, Liang Zhu, Zhi-Yuan Rui, Molecular dynamics simulations of void growth in γ-TiAl single crystal, Comput. Mater. Sci. 84 (2014) 232–237.

[37] Ruicheng Feng, Maomao Wang, Haiyan Li, Yongnian Qi, Qi Wang, Zhiyuan Rui, Micromechanism of cold deformation of two-phase polycrystalline Ti–Al alloy with void, Materials 12 (1) (2019) 184.

[38] Jun Ding, Yu Tian, Lu sheng Wang, Xia Huang, Hao ran Zheng, Kun Song, Xiang guo Zeng, Micro-mechanism of the effect of grain size and temperature on the mechanical properties of polycrystalline TiAl, Comput. Mater. Sci. 158 (2019) 76–87.

[39] Hariprasath Ganesan, Ingo Scheider, Christian J. Cyron, Quantifying the high-temperature separation behavior of lamellar interfaces in γ-titanium aluminide under tensile loading by molecular dynamics, Front. Mater. 7 (2021).

[40] Hariprasath Ganesan, Ingo Scheider, Christian.J. Cyron, Understanding creep in TiAl alloys on the nanosecond scale by molecular dynamics simulations, Mater. Des. 212 (2021) 110282.

[41] Ashish Chauniyal, Rebecca Janisch, How coherent and semi-coherent interfaces govern dislocation nucleation in lamellar TiAl alloys, Adv. Eng. Mater. 25 (15) (2023) 2300121.

[42] Jiyao Liu, Laiqi Zhang, Molecular dynamics simulation of the tensile deformation behavior of the $\gamma(TiAl)/\alpha_2$(Ti3Al) interface at different temperatures, J. Mater. Eng. Perform. 31 (2021) 918–932.

[43] Henggao Xiang, Wanlin Guo, Synergistic effects of twin boundary and phase boundary for enhancing ultimate strength and ductility of lamellar TiAl single crystals, Int. J. Plast. 150 (2022) 103197.

[44] Anupam Neogi, Rebecca Janisch, Unravelling the lamellar size-dependent fracture behavior of fully lamellar intermetallic γ-TiAl, Acta Mater. 227 (2022) 117698.

[45] Beikai Zhao, Peng Huang, Libo Zhang, Suzhi Li, Ze Zhang, Qian Yu, Temperature effect on stacking fault energy and deformation mechanisms in titanium and titanium-aluminium alloy, Sci. Rep. 10 (2020).

[46] C. Liang, W.B. Liu, H.P. Wang, Enhanced tensile properties and intersecting nanotwins formation mechanism of Ti44Al48Nb8 alloy via electromagnetic levitation processing, Int. J. Plast. 159 (2022) 103451.

[47] Yue Gao, Tinghong Gao, Lianxin Li, Quan Xie, Qian Chen, Zean Tian, Yongchao Liang, Bei Wang, Evolution of dislocation and twin structures in Ti3Al during solidification, Vacuum 194 (2021) 110525.
[48] Pengtao Li, Y.Q. Yang, Vladimir Koval, Jianxin Chen, Xian Luo, Wen Zhang, Bowen Wang, Haixue Yan, Temperature-dependent deformation processes in two-phase TiAl+ Ti3Al nano-polycrystalline alloys, Mater. Des. 199 (2021) 109422.
[49] Rong Fu, Zhiyuan Rui, Ruicheng Feng, Yun Dong, Xin Lv, Effects of γ/γ lamellar interfaces on translamellar crack propagation in TiAl alloys, J. Alloys Compd. 918 (2022) 165616.
[50] Julia Panova, Diana Farkas, Atomistic simulation of dislocation core configurations in TiAl, Philos. Mag. A 78 (2) (1998) 389–404.
[51] Julia Panova, Diana Farkas, Atomistic simulation of fracture in TiAl, Metall. Mater. Trans. A 29 (3) (1998) 951–955.
[52] S. Znam, D. Nguyen-Manh, D.G. Pettifor, V. Vitek, Atomistic modelling of TiAl I. Bond-order potentials with environmental dependence, Philos. Mag. 83 (4) (2003) 415–438.
[53] Chr Herzig, T. Przeorski, Y. Mishin, Self-diffusion in γ-TiAl: an experimental study and atomistic calculations, Intermetallics 7 (3–4) (1999) 389–404.
[54] Fei Zhao, Jie Zhang, Chenwei He, Yong Zhang, Xiaolei Gao, Lu Xie, Molecular dynamics simulation on creep behavior of nanocrystalline TiAl alloy, Nanomaterials 10 (9) (aug 2020) 1693.
[55] G.M. Poletaev, Self-diffusion in liquid and solid alloys of the Ti–Al system: molecular dynamics simulation, J. Exp. Theor. Phys. 133 (2021) 455–460.
[56] Chris Jones, Diana Farkas, Embedded atom simulation of the B2 phase in Nb-Ti-Al, Comput. Mater. Sci. 6 (3) (1996) 231–239.
[57] Diana Farkas, Chris Jones, Dislocation core structure in the B2 phase of Nb-40%Ti-15%Al, Comput. Mater. Sci. 6 (4) (1996) 295–302.
[58] Diana Farkas, Atomistic simulations of fracture in the B2 phase of the Nb–Ti–Al system, Mater. Sci. Eng. A 249 (1) (1998) 249–258.
[59] Yan feng Li, Hui Xu, Zhao quan Song, Song shan Ma, Effect of Nb on plasticity and oxidation behavior of TiAlNb intermetallic compound by density functional theory, J. Cent. South Univ. Technol. 17 (4) (2010) 674–682.
[60] Li Ping, Lusheng Wang, Siliang Yan, Miao Meng, Kemin Xue, Temperature effect on the diffusion welding process and mechanism of B2–O interface in the Ti2AlNb-based alloy: a molecular dynamics simulation, Vacuum 173 (2020) 109118.
[61] Shitan Yan, Zhixiang Qi, Yang Chen, Yuede Cao, Jinpeng Zhang, Gong Zheng, Fengrui Chen, Ting Bian, Guang Chen, Interlamellar boundaries govern cracking, Acta Mater. 215 (2021) 117091.
[62] F. Appel, H. Clemens, F.D. Fischer, Modeling concepts for intermetallic titanium aluminides, Prog. Mater. Sci. 81 (2016) 55–124.
[63] David Holec, Neda Abdoshahi, Dominik Gehringer, Lukas Hatzenbichler, Amin Sakic, Helmut Clemens, Electrons meet alloy development: a γ-TiAl-based alloy showcase, Adv. Eng. Mater. 24 (1) (oct 2021) 2100977.
[64] Aidan P. Thompson, H. Metin Aktulga, Richard Berger, Dan S. Bolintineanu, W. Michael Brown, Paul S. Crozier, Pieter J. in 't Veld, Axel Kohlmeyer, Stan G. Moore, Trung Dac Nguyen, Ray Shan, Mark J. Stevens, Julien Tranchida, Christian Trott, Steven J. Plimpton, LAMMPS - a flexible simulation tool for particle-based materials modeling at the atomic, meso, and continuum scales, Comput. Phys. Commun. 271 (2022) 108171.
[65] Pierre Hirel Atomsk, A tool for manipulating and converting atomic data files, Comput. Phys. Commun. 197 (2015) 212–219.
[66] Alexander Stukowski, Visualization and analysis of atomistic simulation data with OVITO–the open visualization tool, Model. Simul. Mater. Sci. Eng. 18 (1) (2009) 015012.
[67] Paolo Giannozzi, Stefano Baroni, Nicola Bonini, Matteo Calandra, Roberto Car, Carlo Cavazzoni, Davide Ceresoli, Guido L. Chiarotti, Matteo Cococcioni, Ismaila Dabo, Andrea Dal Corso, Stefano de Gironcoli, Stefano Fabris, Guido Fratesi, Ralph Gebauer, Uwe Gerstmann, Christos Gougoussis, Anton Kokalj, Michele Lazzeri, Layla Martin-Samos, Nicola Marzari, Francesco Mauri, Riccardo Mazzarello, Stefano Paolini, Alfredo Pasquarello, Lorenzo Paulatto, Carlo Sbraccia, Sandro Scandolo, Gabriele Sclauzero, Ari P. Seitsonen, Alexander Smogunov, Paolo Umari, Renata M. Wentzcovitch, QUANTUM ESPRESSO: a modular and open-source software project for quantum simulations of materials, J. Phys. Condens. Matter 21 (39) (2009) 395502.
[68] G. Kresse, D. Joubert, From ultrasoft pseudopotentials to the projector augmented-wave method, Phys. Rev. B 59 (3) (1999) 1758–1775.
[69] John P. Perdew, Kieron Burke, Matthias Ernzerhof, Generalized gradient approximation made simple, Phys. Rev. Lett. 77 (18) (1996) 3865–3868.
[70] Hendrik J. Monkhorst, James D. Pack, Special points for Brillouin-zone integrations, Phys. Rev. B 13 (12) (1976) 5188–5192.
[71] Takeshi Kawabata, Hideaki Fukai, Osamu Izumi, Effect of ternary additions on mechanical properties of TiAl, Acta Mater. 46 (6) (1998) 2185–2194.
[72] Feng Hao, Rickard Armiento, Ann E. Mattsson, Using the electron localization function to correct for confinement physics in semi-local density functional theory, J. Chem. Phys. 140 (18) (2014) 18A536.
[73] Young-Won Kim, Intermetallic alloys based on gamma titanium aluminide, JOM 41 (7) (1989) 24–30.
[74] Young-Won Kim, Dennis M. Dimiduk, Progress in the understanding of gamma titanium aluminides, JOM 43 (8) (1991) 40–47.
[75] Peng tao Li, Yan-Qing Yang, Wei Zhang, Xian Luo, Na Jin, Gang Liu, Structural evolution of TiAl during rapid solidification processing revealed by molecular dynamics simulations, RSC Adv. 6 (60) (2016) 54763–54767.
[76] Qing-Xiang Pei, M.H. Jhon, Siu Sin Quek, Zhaoxuan Wu, A systematic study of interatomic potentials for mechanical behaviours of Ti-Al alloys, Comput. Mater. Sci. 188 (2021) 110239.
[77] M. Morinaga, J. Saito, N. Yukawa, H. Adachi, Electronic effect on the ductility of alloyed TiAl compound, Acta Metall. Mater. 38 (1) (1990) 25–29.
[78] Y. Song, D.S. Xu, R. Yang, D. Li, Z.Q. Hu, Theoretical investigation of ductilizing effects of alloying elements on TiAl, Intermetallics 6 (3) (1998) 157–165.
[79] Hong-Bo Zhou, Ye Wei, Yue-Lin Liu, Ying Zhang, Guang-Hong Lu, First-principles investigation of site preference and bonding properties of alloying element in TiAl with O impurity, Model. Simul. Mater. Sci. Eng. 18 (1) (2009) 015007.
[80] C.L. Chen, W. Lu, L.L. He, H.Q. Ye, Deformation-induced $\gamma \rightarrow$ DI-α_2 phase transformation occurring in the twin-intersection region of TiAl alloys, J. Mater. Res. 22 (9) (2007) 2416–2422.
[81] J.G. Wang, L.C. Zhang, G.L. Chen, H.Q. Ye, T.G. Nieh, Deformation-induced $\gamma \leftrightarrow \alpha 2$ phase transformation in a hot-forged Ti-45Al-10Nb alloy, Mater. Sci. Eng. A 239–240 (1997) 287–292.
[82] C.L. Chen, W. Lu, L.L. He, H.Q. Ye, First-principles study of deformation-induced phase transformations in Ti-Al intermetallics, J. Mater. Res. 24 (5) (2009) 1662–1666.
[83] Kun Zhao, Yong Liu, Tianhang Yao, Bin Liu, Yuehui He, Surface nanocrystallization of Ti-45Al-7Nb-0.3W intermetallics induced by surface mechanical grinding treatment, Mater. Lett. 166 (2016) 59–62.
[84] Guoming Zheng, Bin Tang, Wei Chen, Songkuan Zhao, Yizhen Xie, Xiaofei Chen, Jinshan Li, Lei Zhu, Long-period stacking ordering induced ductility of nanolamellar TiAl alloy at elevated temperature, Mater. Res. Lett. 11 (6) (2023) 414–421.
[85] Daosheng Wen, Beibei Kong, Shouren Wang, Lihua Liu, Qiang Song, Ziqiang Yin, Mechanism of stress- and thermal-induced fct → hcp → fcc crystal structure change in a TiAl-based alloy compressed at elevated temperature, Mater. Sci. Eng. A 840 (2022) 143011.
[86] J.D.H. Paul, F. Appel, R. Wagner, The compression behaviour of niobium alloyed γ-titanium alumindies, Acta Mater. 46 (4) (1998) 1075–1085.